PHYSICAL REVIEW B **87**, 115109 (2013)

Non-Drude universal scaling laws for the optical response of local Fermi liquids

Christophe Berthod,[1] Jernej Mravlje,[2,3,4] Xiaoyu Deng,[5] Rok Žitko,[4] Dirk van der Marel,[1] and Antoine Georges[1,2,3]

[1]*Département de Physique de la Matière Condensée, Université de Genève, 24 quai Ernest-Ansermet, 1211 Genève 4, Switzerland*

[2]*Collège de France, 11 place Marcelin Berthelot, 75005 Paris, France*

[3]*Centre de Physique Théorique, École Polytechnique, CNRS, 91128 Palaiseau, France*

[4]*Jožef Stefan Institute, Jamova 39, Ljubljana, Slovenia*

[5]*Department of Physics, Rutgers University, Piscataway, New Jersey 08854, USA*

(Received 26 December 2012; revised manuscript received 25 February 2013; published 7 March 2013)

We investigate the frequency and temperature dependence of the low-energy electron dynamics in a Landau Fermi liquid with a local self-energy. We show that the frequency and temperature dependencies of the optical conductivity obey universal scaling forms, for which explicit analytical expressions are obtained. For the optical conductivity and the associated memory function, we obtain a number of surprising features that differ qualitatively from the Drude model and are universal characteristics of a Fermi liquid. Different physical regimes of scaling are identified, with marked non-Drude features in the regime where $\hbar\omega \sim k_B T$. These analytical results for the optical conductivity are compared to numerical calculations for the doped Hubbard model within dynamical mean-field theory. For the "universal" low-energy electrodynamics, we obtain perfect agreement between numerical calculations and analytical scaling laws. Both results show that the optical conductivity displays a non-Drude "foot," which could be easily mistaken as a signature of breakdown of the Fermi liquid, while it actually is a striking signature of its applicability. The aforementioned scaling laws provide a quantitative tool for the experimental identification and analysis of the Fermi-liquid state using optical spectroscopy, and a powerful method for the identification of alternative states of matter, when applicable.

DOI: 10.1103/PhysRevB.87.115109 PACS number(s): 78.20.Bh, 78.47.db, 72.15.Lh

I. INTRODUCTION

A century after its elaboration, the Drude formula is still commonly used to analyze the electrodynamic response of metals.[1,2] However, the conceptual basis underlying Drude's phenomenological description has been entirely changed by the modern quantum theory of the solid state. The key point is the emergence of long-lived quasiparticle excitations at low energy and low temperature, which are the actual charge carriers in good metals. Understanding the emergence of quasiparticles from a correlated liquid of interacting electrons is the great achievement of Landau's Fermi liquid (FL) theory,[3] which is precisely half as old as the Drude theory. In FL theory, the existence of long-lived quasiparticles is due to the vanishing of their scattering rate as the Fermi surface is approached because of phase-space constraints and the Pauli principle. For quasiparticles to be well defined, however, they must have a relaxation rate smaller than their energy (and hence than the available thermal excitation energy $\sim k_B T$), a condition which is met at low temperatures close to the Fermi surface of simple metals.

When exciting carriers at a low frequency ω, one induces intraband transitions of energy $\hbar\omega$ between states within windows of order $k_B T$, thus probing the relaxation rate up to energies, typically, of $\hbar\omega + k_B T$. A Drude-like response is expected if the relaxation rate does not vary appreciably over this energy range. For Landau quasiparticles in an FL, the relaxation rate increases quadratically with increasing energy and temperature. The conditions for a Drude response are therefore met if $\hbar\omega \ll k_B T$, but deviations are expected if $\hbar\omega \gtrsim k_B T$. Deviations from a pure Drude behavior are actually common in metals, and this is often somewhat loosely interpreted as a violation of Fermi-liquid behavior. However, in order to distinguish non-Drude features that are consistent with—or even signatures of—FL behavior from those that indicate a genuine breakdown of FL theory, one needs to understand the response of Landau quasiparticles to electromagnetic waves. This is a difficult task in general, which has regained interest recently,[4,5] along with the development of low-frequency spectrometers.[6,7]

In this paper, we address this problem in the context of local Fermi liquids. By "local," we mean that the scattering rate, and more generally the single-particle self-energy, is independent of momentum. From a theory viewpoint, local FLs are realized, e.g., in the dynamical mean-field theory (DMFT) of strongly correlated electron models. The assumption of a local self-energy becomes increasingly accurate with increasing coordination number. It is exact in the limit of infinite dimensionality.[8,9] The success of this approach in practice also demonstrates that a weak momentum dependence is a reasonable approximation for a wide class of correlated electron materials, at least in some range of composition, temperature, etc., when spatial correlations are short ranged.

The considerable simplification resulting from locality allows us to derive here analytically a universal scaling form of the optical conductivity in the FL regime. We show that a Drude-like behavior is indeed recovered in the regime $\hbar\omega \ll k_B T$. In contrast, clear departure from Drude behavior is found at higher frequency $\hbar\omega \sim k_B T$ when the frequency dependence of the scattering rate becomes important. Characteristic non-Drude signatures of FL behavior in the optical conductivity are identified in this regime.

We also perform DMFT calculations of the optical conductivity for a microscopic model of a hole-doped Mott insulator. We show that the results accurately obey the FL scaling expressions, and that characteristic non-Drude features of the DMFT optical conductivity in the thermal regime $\hbar\omega \sim k_B T$

are explained by the FL scaling analysis. The model calculation also allows us to clearly identify the limitations and range of applicability of universal FL behavior. Finally, we discuss the conditions for a possible experimental observation of the FL universal scaling laws and FL signatures in optical measurements.

The paper is organized as follows. Section II reviews the Drude theory and its generalizations. In Sec. III, we give the general formula for the optical conductivity of a system with a local self-energy. We then introduce the low-energy expression of the self-energy in a local FL, derive analytically a universal scaling expression for the optical conductivity, and discuss the different regimes of physical relevance. Section IV presents a comparison of the FL scaling laws with DMFT calculations. In Sec. V, we address issues related to the experimental observation of FL scaling laws in the optical conductivity, and discuss in more detail the case of UPd_2Al_3. Our conclusions are given in Sec. VI, and a series of Appendices collect additional material.

II. PRELIMINARIES: DRUDE THEORY AND BEYOND

In the Drude theory of conduction in metals, a single frequency-independent time τ_D governs the relaxation of the current. The assumption is that the current decays exponentially once the electric field has been turned off. The classical equation of motion then leads to the dc conductivity $\sigma_{dc} = ne^2\tau_D/m$, with n the carrier density and m the carrier mass. In the presence of an oscillating electric field, the complex frequency-dependent conductivity $\sigma(\omega) = \sigma_1(\omega) + i\sigma_2(\omega)$ reads

$$\sigma(\omega) = \frac{ne^2}{m}\frac{1}{-i\omega + 1/\tau_D} = \frac{\sigma_{dc}}{1 - i\omega\tau_D}. \tag{1}$$

In many materials, however, especially those with strong electron correlations, a single frequency-independent relaxation time does not provide an accurate description of the experimental data.[10] In order to describe the full frequency dependence of the conductivity, it is convenient to introduce[11] a memory function $M(\omega)$ such that

$$\sigma(\omega) = \frac{i\epsilon_0\omega_p^2}{\omega + M(\omega)}. \tag{2}$$

In this expression, we define the plasma frequency from the sum rule over the whole frequency range:

$$\epsilon_0\omega_p^2 \equiv \frac{2}{\pi}\int_0^\infty d\omega\,\sigma_1(\omega). \tag{3}$$

The complex function $M(\omega) = M_1(\omega) + iM_2(\omega)$ plays the role of a self-energy for the optical response. The definition (3) of ω_p^2 ensures that ω dominates over $M(\omega)$ in the expression of $\sigma(\omega)$ at large frequencies. Indeed, the Kramers-Kronig relations

$$\{\sigma_1(\omega), \sigma_2(\omega)\} = \frac{1}{\pi}\mathcal{P}\!\!\!\!\!\!\int_{-\infty}^{\infty} d\Omega\,\frac{\{-\sigma_2(\Omega), \sigma_1(\Omega)\}}{\omega - \Omega} \tag{4}$$

imply that $\sigma_2(\omega \sim \infty) \sim 2\int_0^\infty d\Omega\,\sigma_1(\Omega)/(\pi\omega)$.

Expression (2) can be cast in a form that is formally analogous to the Drude expression ("generalized Drude model"):

$$\sigma(\omega) = \epsilon_0\omega_p^2\frac{\mathscr{D}(\omega)}{-i\omega + 1/\tau_{opt}(\omega)} \tag{5}$$

with

$$\mathscr{D}(\omega) = \left[1 + \frac{M_1(\omega)}{\omega}\right]^{-1}, \quad \frac{1}{\tau_{opt}(\omega)} = \mathscr{D}(\omega)M_2(\omega). \tag{6}$$

Note that the complex conductivity obeys $\sigma^*(\omega) = \sigma(-\omega)$ under complex conjugation, so that σ_1, M_2, $\mathscr{D}$ (respectively, σ_2, M_1) are even (respectively, odd) functions of frequency. $\mathscr{D}(\omega)$ is often denoted $m/m^*(\omega)$, hence defining an optical effective mass, and $\tau_{opt}(\omega)$ is often written as $\tau^*(\omega)$. At low frequency, $\mathscr{D}(\omega \to 0) = (1 + \partial_\omega M_1|_{\omega=0})^{-1}$ renormalizes the bare plasma frequency and the spectral weight of the Drude peak. In many cases, the frequency dependence of the optical scattering rate $1/\tau_{opt}(\omega)$ at low frequency is mainly determined by $M_2(\omega)$, with $\mathscr{D}(\omega)$ having a milder frequency dependence (see below).

When analyzing experimental data, the imaginary part of the memory function, which controls the optical scattering rate, can, for example, be determined through

$$M_2(\omega) = \mathrm{Re}\,\frac{\epsilon_0\omega_p^2}{\sigma(\omega)}, \tag{7}$$

with the plasma frequency determined by the sum rule (3).

III. OPTICAL CONDUCTIVITY OF LOCAL FERMI LIQUIDS

We now specialize the discussion to the optical conductivity of *local* Fermi liquids, i.e., systems in which the single-particle self-energy Σ obeys the low-frequency, low-temperature behavior of Landau Fermi-liquid theory and, additionally, does not depend on momentum. This is the case, in particular, of strongly correlated electron models and materials treated in the framework of dynamical mean-field theory.[12]

We first recall the simplifications encountered in the Kubo formalism in this context, and the resulting expression of the optical conductivity. We then show that universal scaling laws emerge in the Fermi liquid regime and discuss these laws in the different physical regimes.

A. General expression of the optical conductivity

When the single-particle self-energy $\Sigma(\varepsilon)$ has no momentum dependence, the Kubo formalism leads to the following general expression of the optical conductivity:

$$\sigma_1(\omega) = \frac{1}{\omega}\int_{-\infty}^{\infty} d\varepsilon\,[f(\varepsilon) - f(\varepsilon + \hbar\omega)] \times \pi\int_{-\infty}^{\infty} d\xi\;\Phi(\xi)\,A(\xi,\varepsilon)A(\xi,\varepsilon + \hbar\omega), \tag{8a}$$

where $f(\varepsilon)$ is the Fermi function, while $\Phi(\xi)$ and $A(\xi,\varepsilon)$ are, respectively, the transport and the one-particle spectral functions, defined in detail below. The derivation of this formula is outlined in Appendix A. The key point is that vertex corrections associated with the current-current correlation function exactly vanish in the case of a local (momentum

independent) theory,[13] so that the conductivity can be entirely expressed in terms of the one-particle self-energy.

Expression (8a) of the optical conductivity applies to a single-band system to which our discussion is limited in this paper for simplicity. The entire information about the band dispersion is encoded in the transport function Φ, defined by

$$\Phi(\xi) = \frac{2e^2}{dL^d} \sum_{\boldsymbol{k}} v_{\boldsymbol{k}}^2 \delta(\xi - \xi_{\boldsymbol{k}}). \tag{8b}$$

In this expression, L is the system size, d is the dimensionality, $\xi_{\boldsymbol{k}} = E_{\boldsymbol{k}} - \mu$ is the dispersion of the noninteracting Bloch band measured from the chemical potential, and $\boldsymbol{v}_{\boldsymbol{k}} = (1/\hbar)\nabla_{\boldsymbol{k}} E_{\boldsymbol{k}}$ is the corresponding group velocity. Many-body effects enter through the single-electron spectral function $A(\xi,\varepsilon)$, which is related to the self-energy $\Sigma(\varepsilon) = \Sigma_1(\varepsilon) + i\Sigma_2(\varepsilon)$ by

$$A(\xi,\varepsilon) = \frac{-\Sigma_2(\varepsilon)/\pi}{[\varepsilon - \xi - \Sigma_1(\varepsilon)]^2 + [\Sigma_2(\varepsilon)]^2}. \tag{8c}$$

In all these expressions, $\varepsilon/\hbar$ designates a frequency, while the momentum dependence of the spectral function stems from $\xi_{\boldsymbol{k}}$.

The transport function $\Phi(\xi)$ is usually a slow function of its argument, in contrast to $A(\xi,\varepsilon)$ which in a Fermi liquid peaks at $\varepsilon \approx \xi$. When the energy dependence of $\Phi(\xi)$ is negligible over the energy range where the spectral functions are appreciable, the second integral in Eq. (8a) reduces to the convolution of two Lorentzian functions, and the real and imaginary parts of the complex conductivity can be recast into the very convenient form[14–16] (see Appendix A)

$$\sigma(\omega) = \frac{i\Phi(0)}{\omega} \int_{-\infty}^{\infty} d\varepsilon \, \frac{f(\varepsilon) - f(\varepsilon + \hbar\omega)}{\hbar\omega + \Sigma^*(\varepsilon) - \Sigma(\varepsilon + \hbar\omega)}. \tag{9}$$

Equation (9) reduces to the Drude formula, Eq. (1), if we put $\Sigma(\varepsilon) \equiv -i\hbar/(2\tau_{\rm D})$ and if $\Phi(0)$ is evaluated using the three-dimensional isotropic electron gas formula.

In the context of a single-band system, the total sum rule as defined from Eq. (3) reads (see Appendix B)

$$\epsilon_0 \omega_p^2 = \int_{-\infty}^{\infty} d\xi \; \Phi(\xi) \left(-\frac{dn}{d\xi}\right) = \frac{2e^2}{d\hbar^2} \langle n(\xi_{\boldsymbol{k}}) \nabla^2 E_{\boldsymbol{k}} \rangle_{\rm BZ}, \tag{10}$$

where $\langle \cdots \rangle_{\rm BZ}$ designates an average over the Brillouin zone and $n(\xi_{\boldsymbol{k}}) = \langle c_{\boldsymbol{k}}^\dagger c_{\boldsymbol{k}} \rangle = \int d\varepsilon \, f(\varepsilon) \, A(\boldsymbol{k},\varepsilon)$ is the momentum distribution of the electrons. In an interacting Fermi liquid, $-dn/d\xi$ is different from a δ function even at zero temperature, hence $\epsilon_0 \omega_p^2$ is, in general, different from $\Phi(0)$. For a simple tight-binding band $E_{\boldsymbol{k}} \propto \sum_\alpha \cos k_\alpha$, the right-hand side becomes proportional to the kinetic energy. Note that the value of the sum rule thus depends on temperature and interaction strength. This is in contrast to the case where the whole solid (with all bands) is considered, in which case the plasma frequency ω_p^2 is set by the bare electron mass and total number of electrons (f-sum rule). Note also that the approximate formula (9), in which the transport function was replaced by a constant, does not reproduce correctly the total sum rule, which is expected since it is only valid at low energy. We shall see, however, that it can, in general, be used to reliably estimate the spectral weight of the Drude peak.

B. Scattering in a local Fermi liquid

At low frequency and temperature, the self-energy of a local Fermi liquid can be written in the form

$$\Sigma(\varepsilon,T) = \left(1 - \frac{1}{Z}\right)\varepsilon - \frac{i}{Z\pi k_{\rm B} T_0}[\varepsilon^2 + (\pi k_{\rm B} T)^2]. \tag{11}$$

In this expression, Z is the quasiparticle spectral weight. In a local Fermi liquid, it is also related to the quasiparticle mass renormalization through $Z = m/m^*$ (i.e., the quasiparticle Fermi velocity is $v_{\rm F}^* = Z v_{\rm F}$). Close to the Fermi surface and for $\varepsilon \ll k_{\rm B} T$, the spectral function is approximately a Lorentzian peak of weight Z, centered around $\varepsilon = Z\xi_{\boldsymbol{k}}$ (the quasiparticle dispersion). We define the temperature-dependent quasiparticle lifetime from the zero-frequency value of Σ_2 as

$$\frac{\hbar}{\tau_{\rm qp}} \equiv 2Z|\Sigma_2(\varepsilon = 0,T)| = 2\pi \frac{(k_{\rm B} T)^2}{k_{\rm B} T_0}. \tag{12}$$

It corresponds to twice the width of the Lorentzian quasiparticle peak in the spectral function, that is, to the decay rate of the probability (square of the Green's function).

Fermi liquid behavior self-consistently relies on the existence of a sharp Fermi surface and applies when the scattering rate of the typical excitation is smaller than its energy. The scattering rate $\hbar/\tau_{\rm qp}$ must be compared to a typical thermal excitation energy, say $2\pi k_{\rm B} T$. The characteristic Fermi liquid energy scale $k_{\rm B} T_0$ is defined as the temperature where $\hbar/\tau_{\rm qp} = 2\pi k_{\rm B} T$ and will serve as a basic unit below. This is illustrated in Fig. 1 (left panel), which sketches the dependence of the quasiparticle lifetime on temperature. The temperature T_0 also sets the coupling strength: a small T_0 corresponds to strong electron-electron interactions and a large value of Σ_2. Hence the quasiparticle lifetime diminishes rapidly as a function of temperature and frequency. The precise relation of the scale T_0 to the scale $T_{\rm FL}$, below which strict Fermi liquid behavior holds, is discussed in Sec. IV. In strongly correlated (local) Fermi liquids in which Z is small, e.g., close to a Mott transition (see Sec. IV) or in heavy-fermion materials, all physical quantities scale with a single energy scale, and T_0 is proportional to $\sim ZD$ (with possibly a small value of the prefactor). Here, D is the half-bandwidth of the bare band.

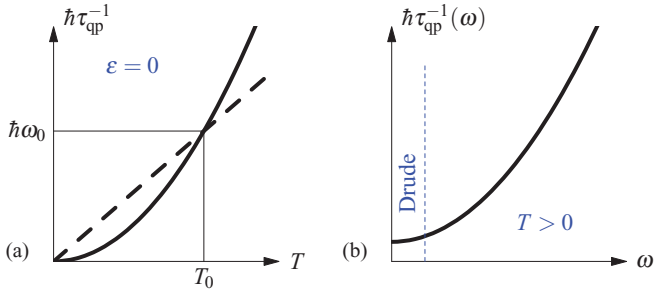

FIG. 1. (Color online) Fermi liquid scattering rate $\hbar\tau_{\rm qp}^{-1}$. (a) At zero energy, $\hbar\tau_{\rm qp}^{-1}$ increases quadratically with temperature (solid line). The dashed line indicates $2\pi k_{\rm B} T$. The intercept defines a temperature scale T_0 and a frequency scale $\hbar\omega_0 = 2\pi k_{\rm B} T_0$. (b) At finite T, $\hbar\tau_{\rm qp}^{-1}(\omega)$ increases quadratically with the frequency ω. The applicability of the frequency-independent (Drude) approximation is limited to low frequencies.

The factor $1/Z$, which has been pulled out in front of Σ_2 in order to define T_0, ensures that in such a case Σ_2 is a scaling function of T/ZD and ε/ZD.

The right panel of Fig. 1 suggests that the frequency dependence of the quasiparticle scattering rate is actually important. A Drude-like optical response with a constant relaxation time $\tau_D \sim \tau_{qp}$ can only be expected to provide a reasonable description in the very low-frequency or relatively high-temperature regime $\hbar\omega \lesssim 2\pi k_B T$. When $\hbar\omega \gtrsim 2\pi k_B T$, the energy dependence of $\Sigma(\varepsilon)$ cannot be neglected and a non-Drude response arises, as discussed in the following section.

We finally note that a real, frequency-independent Hartree term $\Sigma_1(0,T)$ should in fact be added to Eq. (11) for completeness. It sets the location of the Fermi surface from $E_k = \mu - \Sigma_1(0,T)$ and can be viewed as a shift of the chemical potential, which will be omitted for simplicity in all equations. An imaginary frequency-independent part can also be added to mimic the effects of the impurity scattering. This is considered in Appendix F.

C. Scaling form of the optical conductivity in a local Fermi liquid

We now show that the optical conductivity obeys a universal scaling form in terms of the two variables $\omega\tau_{qp}$ and $\hbar\omega/(2\pi k_B T)$. Whereas it reduces essentially to the Drude form in the low-frequency limit, its full frequency dependence is markedly different.

The universal scaling form is derived by inserting Eq. (11) into Eq. (9). The calculations can be performed analytically and yield

$$\sigma(\omega) = \sigma_{dc}\,\mathscr{S}\left(\frac{\hbar\omega}{2\pi k_B T}, \omega\tau_{qp}\right), \tag{13a}$$

$$\sigma_{dc} = \frac{\pi^2}{12} Z\Phi(0)\tau_{qp}, \tag{13b}$$

$$\mathscr{S}(x,y) = \frac{6}{\pi^2 x}\int_{-\infty}^{\infty} du\, \frac{[e^{\pi(u-x)}+1]^{-1} - [e^{\pi(u+x)}+1]^{-1}}{1+x^2-iy+u^2}.$$

The scaling function $\mathscr{S}$ is evaluated and displayed in Appendix C. One obtains

$$\mathscr{S}(x,y) = \frac{6i}{\pi^2}\frac{1}{x\,r(x,y)}\left\{\psi\left(\frac{1}{2}[1+r(x,y)-ix]\right) - \psi\left(\frac{1}{2}[1+r(x,y)+ix]\right)\right\}, \tag{13c}$$

where $r(x,y) = \sqrt{1+x^2-iy}$ and ψ is the digamma function defined as $\psi(z) = \lim_{M\to\infty}[\ln M - \sum_{n=0}^{M} 1/(n+z)]$.

Equation (13a) emphasizes the emergence of two natural time/frequency scales: the quasiparticle time τ_{qp}, and a "coherence" time $\hbar/(2\pi k_B T)$. Alternatively, one can reexpress

$$\sigma(\omega) = \sigma_{dc}\,\mathscr{S}\left(\frac{\bar\omega}{\bar T}, \frac{\bar\omega}{\bar T^2}\right) \tag{14}$$

with $\bar\omega \equiv \hbar\omega/(2\pi k_B T_0)$ and $\bar T \equiv T/T_0$ dimensionless variables normalized to the basic scale T_0. This emphasizes that the optical conductivity in a Fermi liquid is a scaling function of ω/T and ω/T^2. Equations (13) constitute the key analytical result of this article. They replace the Drude formula by a universal scaling form of these *two* frequency scales, which is valid for local Fermi liquids. Let us emphasize that all high-energy scales such as the bare bandwidth or the plasma frequency ω_p have disappeared from the scaling expression (13). Instead, only low-energy scales appear, such as T_0 and $Z\Phi(0)$ (the latter is shown below to be related to the low-energy Drude weight).

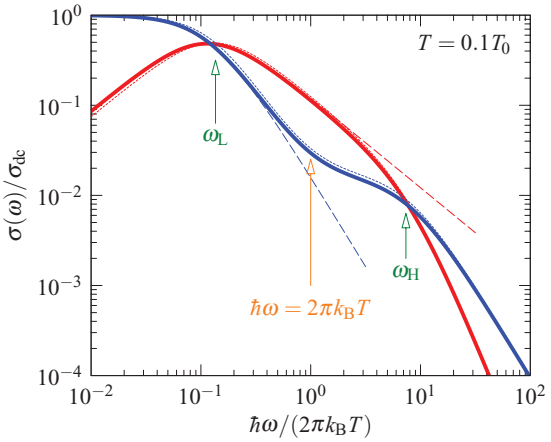

FIG. 2. (Color online) Fermi-liquid conductivity (13) at low temperature (solid lines), below the temperature T_1 defined in Fig. 3. The blue (red) lines show the real (imaginary) part of the conductivity. The dashed lines show the low-frequency Drude-like behavior given by Eq. (15). The dotted lines show Eq. (18). The characteristic frequency scales ω_L and ω_H correspond to those defined in Fig. 3 and Eq. (20).

In Fig. 2, we plot the real and the imaginary parts of $\sigma(\omega)/\sigma_{dc}$ as a function of $\hbar\omega/(2\pi k_B T)$ on a log-log scale at a given low temperature $T/T_0 = 0.1$. (The full frequency and temperature dependencies are shown on a three-dimensional plot in Appendix C.) Three frequency regimes can be identified from this plot. (1) At low-frequency $\omega \lesssim \omega_L < 2\pi k_B T/\hbar$ (with ω_L to be made precise below, of order τ_{qp}^{-1} at low temperature), the conductivity follows closely the Drude model, with a saturation of σ_1 below the characteristic frequency τ_{qp}^{-1} and a $1/\omega^2$ decay above it. τ_{qp}^{-1} also separates the dissipative regime (with larger σ_1) from the inductive regime (with larger σ_2).

(2) When ω approaches $2\pi k_B T/\hbar$, the conductivity deviates from the Drude behavior: σ_1 displays a pronounced shoulder with much weaker frequency dependence—the feature appears as a shoulder in a log-log plot, as a "foot" in a lin-lin plot, see below. In this "thermal" regime, the conductivity behaves inductively ($\sigma_2 > \sigma_1$) rather than dissipatively.

(3) Increasing ω further, leads to a more rapid decay of σ_2, and at ω_H (to be defined below), the data become dissipative-like again ($\sigma_1/\sigma_2 > 1$). This is actually a consequence of the assumed unbounded quadratic increase of the scattering rate with frequency, and might not be physical in this already high-frequency regime (see Sec. IV). Above ω_H, σ_1 recovers a Drude-like $1/\omega^2$ decay, while σ_2 turns to $1/\omega^3$. The $1/\omega^3$ behavior is an artifact of extending the ω^2 in the self-energy (11) to high energies.[17]

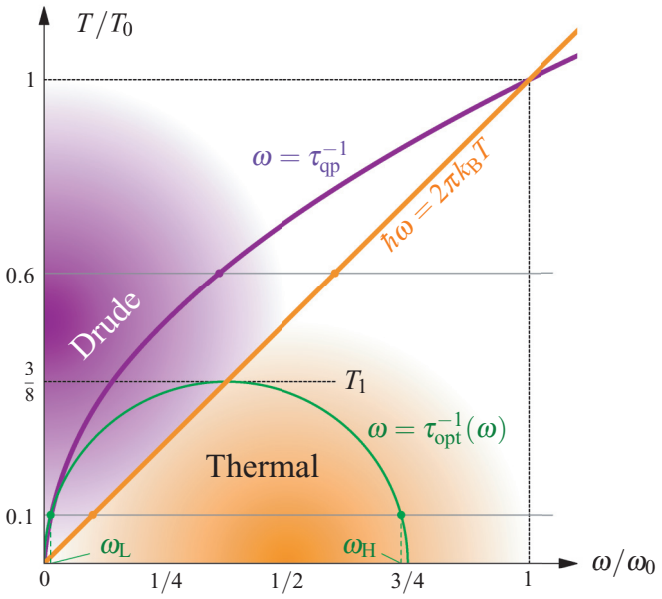

FIG. 3. (Color online) Regimes of conduction. The Drude regime applies if $\omega < 2\pi k_B T/\hbar$, and the thermal regime if $\omega \gtrsim 2\pi k_B T/\hbar$. The conductivity along the two horizontal cuts at fixed temperature is displayed in Figs. 2 and 6.

These different regimes, as well as the precise conditions determining the characteristic frequencies $\omega_{L,H}$ are represented on Fig. 3. We now discuss these different regimes in more detail.

D. Drude regime

The lowest frequency regime can legitimately be called "Drude regime," since there the frequency dependence of the scattering rate can be ignored. In this regime, the frequency $\hbar\omega$ is small with respect to $2\pi k_B T$, the inverse quasiparticle time τ_{qp}^{-1} is smaller than, or comparable to the temperature, but the product $\omega\tau_{qp} \equiv y$ can take arbitrary values (see Fig. 3). This regime is thus described by taking the limit $x \equiv \hbar\omega/(2\pi k_B T) \to 0$ in the scaling form (13c). This yields

$$\frac{\sigma(\omega)}{\sigma_{dc}} \approx \frac{6}{\pi^2} \frac{\psi'\left(\frac{1}{2}[1+\sqrt{1-i\omega\tau_{qp}}]\right)}{\sqrt{1-i\omega\tau_{qp}}}, \tag{15}$$

where ψ' is the derivative of the digamma function. This is shown as the dashed lines in Fig. 2. Interestingly, this expression differs from the simple Drude form $\sigma(\omega)/\sigma_{dc} = 1/(1-i\omega\tau_D)$. However, as detailed in Appendix D, the frequency dependence of the exact expression (15) can be rather accurately approximated by the simple Drude form, provided τ_D is chosen in an appropriate manner (which is such that τ_D *differs* from τ_{qp}, however).

The spectral weight in the Drude peak can be estimated as

$$\frac{2}{\pi}\int_0^{\omega_D} d\omega\, \sigma_1(\omega) = Z\Phi(0), \tag{16}$$

in which ω_D is a cutoff defining the Drude regime. This expression can be established in two ways. The first is to perform a direct frequency integration of the scaling expression (15) over the whole frequency range (i.e., for the scaling variable $y = \omega\tau_{qp}$ varying from 0 to ∞). Alternatively, since $\Phi(\xi)$ can be taken as constant in the low-frequency range, one can use expression (9) and observe that it yields a high-frequency behavior of $\sigma_2 \sim Z\Phi(0)/\omega$. By Kramers-Kronig, this leads to Eq. (16).

Two remarks are in order regarding expression (16). First, the Drude weight scales with the quasiparticle weight Z. Close to a Mott transition, for example, Z is expected to vanish and so does the Drude weight. Second, it should be noted that Z measures the renormalization of the Drude weight as compared to the noninteracting (band) value $\Phi(0)$ and *not* the spectral weight of the Drude peak relative to the total integrated spectral weight $\epsilon_0\omega_p^2$. The latter relative weight is given by $Z\Phi(0)/(\epsilon_0\omega_p^2) \approx \mathscr{D}(0)$ with $\epsilon_0\omega_p^2$ given by Eq. (10).

E. Thermal regime and emergence of the 2π factor in the optical scattering rate

In the thermal regime, $\hbar\omega$ is comparable to $2\pi k_B T$ and $\omega\tau_{qp} \gg 1$. This corresponds to the limit of fixed $x = \hbar\omega/(2\pi k_B T)$ and large $y = \omega\tau_{qp} \gg x$. The scaling function $\mathscr{S}(x,y)$ has the following expansion for $y \to \infty$:

$$\mathscr{S}(x, y\to\infty) = \frac{12i}{\pi^2 y} + \frac{16}{\pi^2 y^2}(1+x^2). \tag{17}$$

Using this expression and performing a large-y expansion of $1/\sigma = 1/[\sigma_{dc}\mathscr{S}(x,y)]$, one directly obtains a generalized Drude form for the optical conductivity:

$$\sigma(\omega) \approx \frac{Z\Phi(0)}{-i\omega + 1/\tau_{opt}(\omega)}, \tag{18}$$

with the optical scattering rate

$$\frac{\hbar}{\tau_{opt}(\omega)} = \frac{2}{3\pi k_B T_0}[(\hbar\omega)^2 + (2\pi k_B T)^2]. \tag{19}$$

The same result is found by approximating $\mathscr{D}(\omega)$ in Eq. (5) by $\mathscr{D}(0) \approx Z\Phi(0)/(\epsilon_0\omega_p^2)$, identifying with Eq. (13) and expanding for large y. Equation (18) is displayed in Fig. 2 as the dotted lines. While the Fermi-liquid form of the quasiparticle lifetime (a one-particle quantity) involves $(\hbar\omega)^2 + (\pi k_B T)^2$, it should be emphasized that the optical scattering rate (a two-particle quantity) involves instead a factor 2π in the combination $(\hbar\omega)^2 + (2\pi k_B T)^2$. This was emphasized by Gurzhi in Ref. 18. Experimentally, the 2π factor has not been observed so far in simple metals. As discussed in detail in Sec. V, in several correlated metals, a scaling of the optical scattering rate following $(\hbar\omega)^2 + (p\pi k_B T)^2$ was reported, with values of p ranging from 1 to 2.4.[19–24] The departure from the Fermi-liquid value $p = 2$ may be attributed to scattering mechanisms with a different frequency/temperature dependence.[4,5] In Appendix F, we show that a frequency-independent scattering rate does not change the value $p = 2$.

At low temperature, Eqs. (18) and (19) allow to define two characteristic frequencies $\omega_{L,H}$ from the condition $\omega = \tau_{opt}^{-1}(\omega)$, or equivalently $\sigma_1(\omega) = \sigma_2(\omega)$:

$$\hbar\omega_{L,H} = \frac{3}{4}\pi k_B T_0\left[1 \pm \sqrt{1-\left(\frac{8T}{3T_0}\right)^2}\right]. \tag{20}$$

Plotted as a function of T, these two frequencies form a dome in the (ω, T) plane, defining the thermal regime (green line in

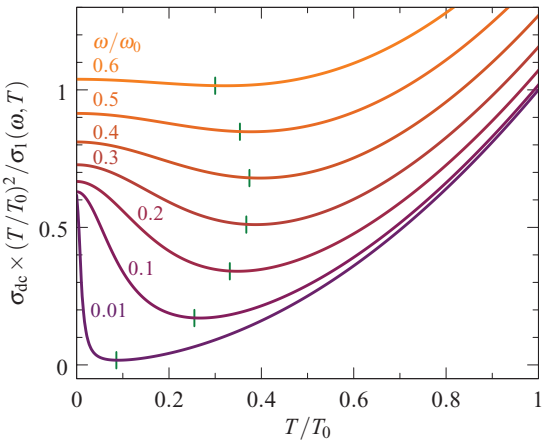

FIG. 4. (Color online) ac resistivity $1/\sigma_1(\omega,T)$ as a function of T for several frequencies ω. These curves correspond to vertical slices in Fig. 3, and the green bars indicate the temperature at which the dome is crossed for each frequency. The temperatures are measured in units of T_0, and the frequencies in units of $\omega_0 = 2\pi k_B T_0/\hbar$. The normalization of the resistivity is $\sigma_{dc}(T/T_0)^2 = \pi\hbar Z\Phi(0)/(24k_B T_0)$.

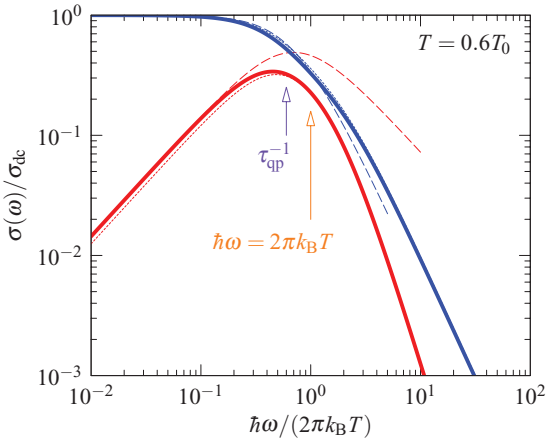

FIG. 6. (Color online) Fermi-liquid conductivity Eq. (13) at high temperature (solid lines), above the temperature T_1 defined in Fig. 3. The blue (red) lines show the real (imaginary) part of the conductivity. The dashed lines show the low-frequency Drude-like behavior given by Eq. (15). The dotted lines show Eq. (18).

Fig. 3). Below this dome, the conductivity behaves inductively. While the scales $\omega_{L,H}$ can be determined from the crossings of σ_1 and σ_2 plotted as a function of frequency (see Fig. 2), the crossing of the dome is most easily identified by a minimum in a plot of $1/\sigma_1(\omega,T)$ as a function of T, at a fixed finite frequency. This is illustrated in Fig. 4. As this determination of $\omega_{L,H}$ only relies on σ_1, it might be the most direct way of checking FL behavior in experimental data sets.

Finally, we plot in Fig. 5 the imaginary part of the memory function, defined according to Eq. (2) with the conductivity given by the Fermi-liquid expressions (13). Figure 5(a) displays the crossover from the Drude to the thermal regime. $M_2(\omega)$ increases quadratically for $\omega \to 0$, with a temperature-dependent curvature given in Appendix E. In the thermal regime, the expansion (17) leads to the following form:

$$M(\omega) \approx \left(\frac{1}{\tilde{Z}} - 1\right)\omega + i\frac{1}{\tilde{Z}}\frac{2}{3\pi\hbar k_B T_0} \times [(\hbar\omega)^2 + (2\pi k_B T)^2], \tag{21}$$

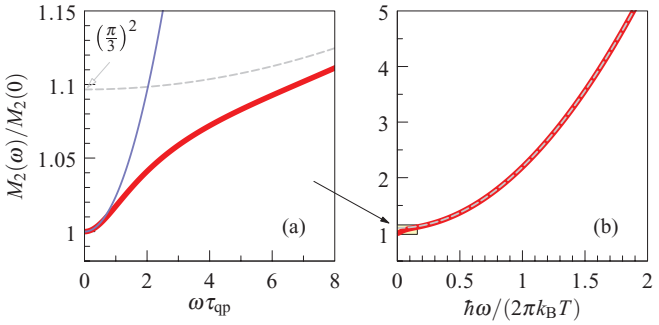

FIG. 5. (Color online) Imaginary part of the memory function in a Fermi liquid at $T = 0.02T_0$ (thick red lines). (a) At frequencies $\omega < \tau_{qp}^{-1}$, $M_2(\omega)$ increases as ω^2 (thin blue line), with a temperature-dependent curvature given by Eq. (E2). (b) In the thermal regime, $M_2(\omega)/M_2(0)$ scales as $(\pi/3)^2(1+x^2)$ with $x = \hbar\omega/(2\pi k_B T)$ (dashed line).

where $\tilde{Z} = Z\Phi(0)/(\epsilon_0\omega_p^2)$. The imaginary part is shown in Fig. 5(b). At $\omega = 0$, Eq. (21) extrapolates to a value larger than the exact value $iM_2(0)$ by a factor $(\pi/3)^2$ (see Appendix E). Similarly, the approximations (18) and (19) for the conductivity deviate slightly from the exact conductivity in the limit $\omega \to 0$. Setting $\omega = 0$ in these equations yields $\sigma(0) = (3/\pi)^2\sigma_{dc}$. All these observations are due to the fact that the expressions (19) and (21) hold in the thermal regime, but are not accurate at very low frequencies.

F. Coherent and "incoherent" regimes

It is seen from Fig. 3 that the three frequency scales $\omega_{L,H}$ and $2\pi k_B T/\hbar$ defined above merge when the temperature is raised above $T_1 = 3T_0/8$. Above T_1, an "incoherent" regime is found in which the thermal scale $2\pi k_B T/\hbar$ becomes the only characteristic frequency scale and σ_2 becomes smaller than σ_1 at all frequencies, because $\tau_{opt}^{-1} > \omega$ (see Fig. 6). The term incoherent is put in quotes, because at such a high temperature $T \sim T_0$ the scaling form of the self-energy may be no longer valid. The actual incoherent regime occurs due to the breakdown of the Fermi liquid form (11) altogether. The question whether the scaling form applies is then irrelevant.

The reciprocal argument, on the other hand, is valid. Observing two frequencies at which $\sigma_1 = \sigma_2$ indicates that the Fermi liquid range has been reached. On a log-log plot of $\omega\sigma_1(\omega)$ versus ω, these two crossing points coincide with two symmetric maxima located at $\omega_{L,H}$, separated by a minimum at $\omega = 2\pi k_B T/\hbar$.

IV. OPTICAL CONDUCTIVITY OF A HOLE-DOPED MOTT INSULATOR WITHIN DYNAMICAL MEAN-FIELD THEORY

A. Model and methods

In this section, we present calculations of the optical conductivity for a specific microscopic model, the single-band Hubbard model of a hole-doped Mott insulator. The calculations are performed within single-site dynamical

mean-field theory (DMFT).[25] As we shall see, the universal scaling form derived above allows one to identify specific signatures of Fermi-liquid behavior in the DMFT optical conductivity, which have not been emphasized previously. Conversely, the model calculation allows for a test of the scaling theory, and especially of its range of validity as a function of frequency and temperature. The optical conductivity has been calculated with DMFT by several authors in various contexts (see, e.g., Refs. 26 and 27, and for a review and more references, Ref. 10). However, an explicit analysis in connection with FL scaling laws has not been made, and such an analysis requires calculations with very high-accuracy solvers at low energy, which became available only recently.

A semicircular density of states with half-bandwidth D has been used, and the model is considered in its paramagnetic phase. The DMFT equations were solved using highly accurate continuous-time quantum Monte Carlo (CT-QMC)[28,29] and numerical renormalization group[30,31] (NRG) solvers. The imaginary-frequency data from Monte Carlo were analytically continued using Padé approximants. Excellent quantitative agreement between the data obtained using the two techniques was achieved in a broad temperature and frequency range. At the lowest temperatures (below $k_B T/D = 0.01$) and the lowest frequencies, however, artifacts associated with the discretization of the energy mesh and spectral broadening become visible in the NRG data, and the CT-QMC + Padé method becomes preferable. Conversely, the CT-QMC + Padé data becomes less accurate at higher temperatures $k_B T/D > 0.05$, especially for larger frequencies $\hbar\omega/D > 1$. The data used here are obtained by taking the low-frequency part ($\hbar\omega/D < 0.15$) from the calculation based on the CT-QMC + Padé self-energies, and the high-frequency part ($\hbar\omega/D > 0.15$) from the NRG self-energies, with perfect matching in the intermediate region.

B. Self-energy, local Fermi-liquid behavior, and key temperature scales

The analysis presented here is based on the DMFT data set used earlier in Ref. 32. There, transport and thermodynamic properties were discussed in detail, but only some aspects of the optical conductivity were addressed. For convenience, we restate here the key temperature scales identified in this previous work, as well as their evolution with doping. The actual data considered in detail later in the present paper are for a doping level $\delta = 20\%$ and a coupling $U/D = 4$ (at which the undoped system is a Mott insulator), but we mention the doping evolution of the key quantities.

The quasiparticle weight Z was found to be approximately equal to the doping level $Z \approx \delta$ (more precisely, $Z = 0.22$ was found for $\delta = 0.2$). A temperature scale of key importance is the Fermi-liquid temperature scale T_{FL}. This was defined as the temperature below which the T^2 behavior of the resistivity and the ω/T scaling of the self-energy apply. From the DMFT data, this scale was identified as $k_B T_{FL} = 0.05\delta D$, which gives $0.01D$ for $\delta = 0.2$, a very low-energy scale. In the same work,[32] the quasiparticle features in the spectra were shown to persist to a much higher temperature, δD. Important particle-hole asymmetry was found in many physical properties. At a scale approximately equal to δD, these

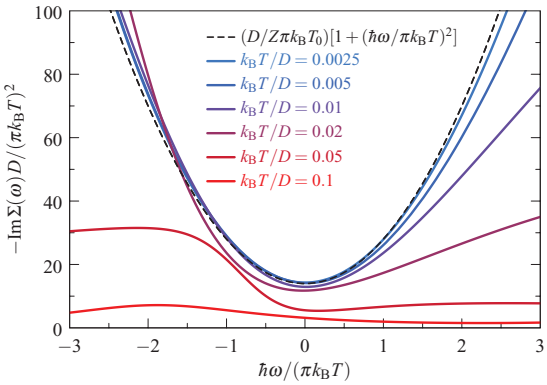

FIG. 7. (Color online) DMFT self-energy scaling plot. At low temperatures, the curves collapse to a parabola. By comparing with Eq. (11) and taking into account that one has $Z = 0.22$ for a doping $\delta = 0.2$, one can determine $k_B T_0 \approx 0.1D \approx 10 k_B T_{FL}$.

"resilient quasiparticles" disappear and the system becomes an incoherent "bad metal" with a resistivity that becomes larger than the Mott-Ioffe-Regel value. It should be emphasized that the Fermi-liquid scale T_{FL} is one order of magnitude smaller than the scale at which the crossover into the bad-metal regime occurs. The latter corresponds quite accurately to the Brinkman-Rice scale $\sim\delta D$, which corresponds to the renormalized kinetic energy of the quasiparticles and is much larger than T_{FL} (although both scales are proportional to the doping level).

In Fig. 7, we display the imaginary part of the self-energies Σ, as a scaling plot $-\mathrm{Im}\,\Sigma(\omega,T)D/(\pi k_B T)^2$ versus $\hbar\omega/(\pi k_B T)$. The data nicely obey the Fermi-liquid law $\propto 1 + (\hbar\omega/\pi k_B T)^2$ at low temperatures. By comparing with the prefactor of this scaling behavior as defined in Eq. (11), one determines the scale T_0 to be (at $\delta = 20\%$) $k_B T_0 \approx 0.1D$, so that $T_0 \approx 10 T_{FL}$. For an arbitrary doping level, one finds, $k_B T_0 \approx 0.57\delta D$. The scale T_0 is thus rather close in magnitude to the Brinkman-Rice scale, while T_{FL} is an order of magnitude smaller. Therefore, when analyzing the DMFT results in the light of Fig. 3 and of the scaling analysis, it should be remembered that FL behavior actually fully applies only below $T_{FL} = 0.1T_0$.

At higher temperatures, deviations from FL rapidly appear for electron-like ($\omega > 0$) single-particle excitations (see Fig. 7). There, the deviations from the parabolic form become substantial at a frequency $\hbar\omega_+ \approx \pi T_{FL}$, where the real part of the self-energy (not shown, see Ref. 32) displays a kink. For holelike excitations ($\omega < 0$), the parabolic behavior is more robust, and the kink appears only at $\omega_- \approx 0.2D$. The transport (resistivity, thermopower) probes a frequency window of a few $k_B T$, and these quantities deviate from the FL universal behavior when $k_B T > \hbar\omega_+$.

C. Optical conductivity at low temperature

Figure 8 for $T = T_{FL}/4 = T_0/40$ demonstrates that the optical conductivity of the hole-doped Hubbard model obtained from DMFT is very well described by the universal FL scaling form (13) derived in the previous section, in the low-frequency and low-temperature regimes. This is indeed

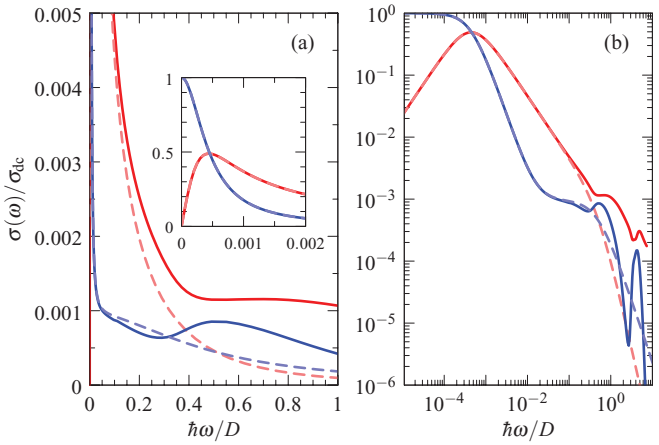

FIG. 8. (Color online) Comparison of the optical conductivity at $k_BT/D = 0.0025D$ ($T = T_{FL}/4$) for the doped Hubbard model calculated within DMFT (solid lines) to the universal FL scaling form (dashed lines). The real (blue) and imaginary (red) parts are plotted on a lin-lin (a) and log-log (b) scale. (Inset) Same data as in (a), showing the Drude-like response in the low-frequency region.

expected from the previous figure demonstrating FL scaling of the single-particle self-energy.

When looking at $\sigma_1(\omega)$ on a lin-lin scale [see Fig. 8(a)], the narrow Drude peak at low-frequency is followed at higher frequency $\hbar\omega \sim 2\pi k_BT$ by a characteristic non-Drude foot. On a log-log plot [see Fig. 8(b)], this appears as a shoulder. This does not signal non-Fermi liquid physics, as one might naively think, but is actually a key feature of FL theory, which signals the onset of the thermal regime at $\hbar\omega \sim 2\pi k_BT$. The non-Drude foot (or shoulder) is thus, somewhat counterintuitively, a striking signature of Fermi-liquid behavior.

At higher frequencies, the DMFT data display two peaks. The first one, for $\hbar\omega \approx 0.5D$ (corresponding typically to the mid-infrared MIR regime) is associated with the transitions between the quasiparticle band and the lower Hubbard band. The high-frequency peak at $\hbar\omega \approx 4D \sim U$ corresponds to the transitions to the upper Hubbard band. These peaks are, obviously, not present in the FL expressions. Likewise, at the highest frequencies, the bare particle dynamics (with $\sigma_2 \propto 1/\omega$) is recovered in the DMFT data, whereas extrapolating FL behavior to infinite frequencies would lead to the incorrect behavior $\sigma_2 \propto 1/\omega^3$.

D. Memory function

More subtle corrections to the FL are seen in the DMFT data, also at frequencies smaller than the MIR, in the foot-shoulder region (but above the low-frequency kink of the self-energy). To resolve them more clearly, it is convenient to look at the memory function. In Fig. 9, we plot the memory function at a low temperature $T = T_{FL}/4$.

The memory function has features on crossing the Hubbard bands [see Fig. 9(a)], which we will not discuss here. Below the MIR scale [see Fig. 9(b)], approximately linear and quadratic behaviors are seen for the real and imaginary parts, respectively [see Fig. 9(c)]. On zooming up further [see Fig. 9(d)], one sees an excellent agreement between the DMFT results and the

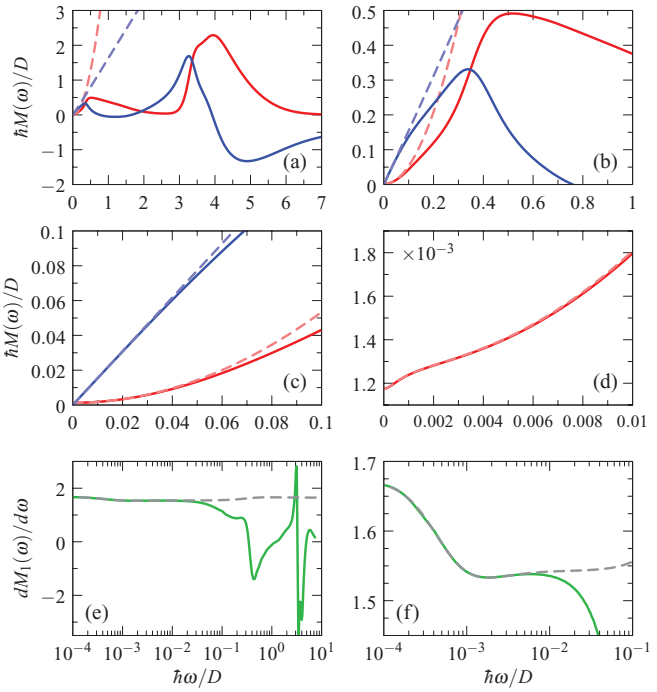

FIG. 9. (Color online) Memory function at $k_BT/D = 0.0025$ ($T = T_{FL}/4$). (a)–(d) Real (solid blue) and imaginary (solid red) parts of the memory function, compared with the FL scaling forms (dashed). The data are shown for several frequency windows ranging from a very broad one (a), to a very narrow one (d). (e) and (f) Frequency derivative of M_1 (solid lines) compared with the FL expressions (dashed lines).

FL scaling form, including the small crossover at the lowest frequency $\omega = 1/\tau_{qp} \approx 0.001$.

Whereas agreement between the DMFT data and the FL scaling form is perfect at the lowest frequencies, some deviations appear at a small but well-defined and important FL frequency scale, the frequency $\omega_+ \approx 0.03$ associated with the positive-energy (electron-like) "kink." This is seen clearly in M_2 or the derivative $dM_1/d\omega$ [see Figs. 9(e) and 9(f)]. The deviation from the FL form goes into the direction of a smaller memory function. This is due to the fact that, in the hole-doped Hubbard model studied here, the positive frequency "resilient quasiparticles" scatter less than the parabolic behavior from Landau FL theory would predict. We stress that, for the hole-doped Hubbard model, the corresponding deviation cannot be observed in photoemission spectroscopy, since they appear at positive excitation energies. Optical spectroscopy, because it probes particle-hole excitations, is thus a powerful tool that could probe the existence of these resilient quasiparticles. Moreover, combining photoemission with precise optical spectroscopy could be used to reveal the strong particle-hole asymmetry of these excitations. Signatures of the low-frequency kink from optical spectroscopy would also be very interesting.

E. Temperature dependence of the optical conductivity

Finally, we discuss the evolution of the optical conductivity at higher temperatures. Figure 10 displays $\sigma_1(\omega)$ for several temperatures ($D/k_BT = 400, 200, 100, 50, 20, 10$). The DMFT

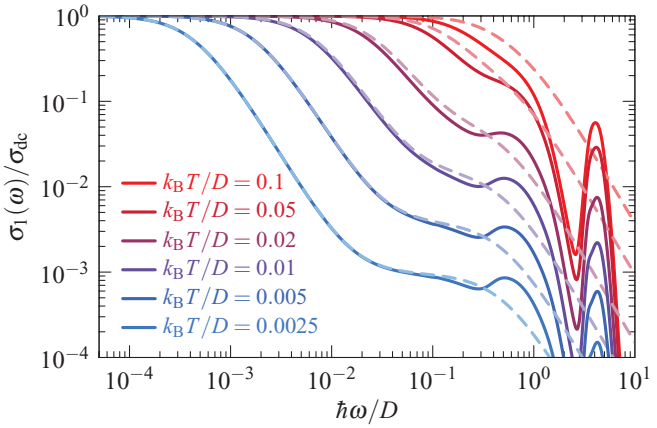

FIG. 10. (Color online) Comparison of the real part of the optical conductivity in the Hubbard model from DMFT (solid lines) with the analytical FL scaling expressions (dashed lines). Inverse temperatures are $D/k_BT = 400, 200, 100, 50, 20, 10$.

data are compared to the analytical form dictated by the FL scaling function, in which τ_{qp} is determined from the FL T^2 dependence. The difference between the FL and the DMFT becomes pronounced for $T \gtrsim T_{FL}$. Note that a milder frequency dependence is seen above T_{FL}, both in the FL and DMFT (in the former it occurs due to the narrowing of the thermal crossover foot-shoulder). This warns again that interpreting apparent non-Drude power laws as a signature of non-Fermi liquid behavior is a risky enterprise.

In Fig. 11, we show the temperature evolution of the imaginary part of the memory function. In Fig. 11(b), the data are plotted as M_2/T^2 versus ω/T. This reveals clearly the scaling behavior, consistent with the $(\hbar\omega)^2 + (2\pi k_BT)^2$ dependence in the thermal regime of FL theory.

At low T, FL deviations from the quadratic dependence on frequency are seen at the lowest frequencies, indicating the onset of the Drude regime where $\hbar\omega \ll 2\pi k_BT$. On the high-energy side, discrepancies are seen above ω_+. Above T_{FL} the data deviate from a parabola and the ω/T FL scaling does not apply anymore.

F. Relation to previous DMFT work

The optical conductivity of doped Mott insulators has been investigated in several earlier single-site DMFT studies (see, e.g., Refs. 26, 27, and 33–35). The main features discussed above appearing in the optical conductivity (the low-frequency peak, the MIR feature associated with transitions involving the lower Hubbard band, and the high-energy feature associated with the upper Hubbard band) agree with these previous works. On the other hand, the precise low-frequency dependence of the optical conductivity has not been discussed previously. The existence of a "thermal" regime when $\hbar\omega \sim k_BT$, and the associated non-Drude foot in $\sigma_1(\omega)$, which is a distinctive signature of Fermi-liquid behavior, as well as the universal scaling form describing the low-frequency regime, were not reported in previous literature using DMFT. The technical reason is that these can only be revealed when using high-accuracy impurity solvers in order to produce accurate data for the self-energy on the real-frequency axis at low temperature. Such techniques only became available recently.

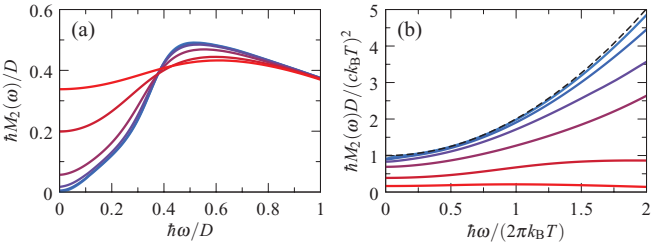

FIG. 11. (Color online) (a) Temperature dependence of the imaginary part of the memory function in DMFT. The temperatures and the color code are the same as in Fig. 10. (b) Scaling plot. The $\hbar\omega/(2\pi k_BT)$ scaling applies at low temperatures and intermediate frequencies. The dashed line shows the parabolic behavior corresponding to Eq. (21).

Obviously, an important open issue raised by our work is the influence of spatial correlations beyond single-site DMFT, and their consequences for the scaling behavior and the features pointed out here. Answering this question requires two major steps on the methodological level. First, the momentum dependence of the self-energy must be taken into account, for example, using cluster extensions of DMFT. Second, one must consider the possible influence of vertex corrections, which cannot be discarded whenever the self-energy has momentum dependence. These are active fields of current research, which go well beyond the simple framework and observations of the present article. Some recent studies have pioneered the investigation of vertex corrections to the optical conductivity, such as Refs. 36–38. To what extent the results reported here survive in the presence of strong spatial correlations is an interesting and challenging open problem. It will demand more work on the methodological and technical sides to provide accurate access to the low-temperature, low-frequency regimes of interest to our study. In this respect, let us remark that the studies based on exact diagonalization and related approaches do not provide access to this regime (see, e.g., Ref. 39), since they apply to finite-size systems and hence have a limited frequency resolution.

V. IMPLICATIONS FOR EXPERIMENTS

In this section, we address the implications for the experimental optical signatures of Fermi-liquid behavior, in the light of the theoretical results discussed in Sec. III. We will also discuss what has been obtained until now in a number of materials, in particular, the heavy-fermion materials $CePd_3$, UPd_2Al_3, and URu_2Si_2, helimagnetic MnSi, the organic conductor κ-(BEDT-TTF)$_2$Cu[N(CN)$_2$]Br$_x$Cl$_{1-x}$, the doped semiconductor $SrTiO_3$, and the doped Mott-Hubbard insulator $HgBa_2CuO_{4+\delta}$. We will see that the experimental optical data published until now do not provide a sufficiently broad spectral range to distinguish all of the optical features of a Fermi liquid. The first signature is the foot (or shoulder), illustrated in Figs. 2 and 8, which marks the deviation from a low-frequency Drude-like behavior. This feature occurs at the frequency $\omega \sim 2\pi k_BT/\hbar$—in-between two frequencies where the imaginary and real parts of the conductivity are equal—and disappears as the temperature is raised above T_1 (see Figs. 3 and 6). The second signature is the characteristic

frequency-temperature scaling of the optical relaxation rate shown in Eq. (19), or the equivalent behavior of the memory function given in Eq. (21). While the first signature can, in principle, be observed in the raw data, the second requires a determination of the spectral weight in order to invert the complex conductivity. A third signature—present in the raw data—is the minimum in $1/\sigma_1$, when plotted as a function of temperature at finite frequency (see Fig. 4).

Experimentally, the most direct clue of Fermi-liquid physics is a T^2 law in the resistivity. This is usually observed between a ground-state ordering temperature T_c, and a scale $T_{\rm FL}$ above which additional scattering mechanisms contribute to the resistivity with a different temperature dependence. For $T_c < T < T_{\rm FL}$, Fermi-liquid signatures are expected in the conductivity (provided $T < T_1 = 3T_0/8$) around the frequency $\nu = k_{\rm B}T/\hbar$, which is ∼1.3 THz for $T = 10$ K, corresponding to 44 cm^{-1}. The signature may be masked by optical phonons—with energies typically above 5 meV, i.e., 1 THz or 40 cm^{-1}—and interband transitions. Another possible limitation is impurity scattering, which reduces the value of T_1 as discussed in Appendix F.

Fermi-liquid behavior of the dc resistivity has been reported in a variety of materials. Using a bolometric direct absorption technique, Webb *et al.*[40] observed the narrow zero-frequency mode corresponding to the Drude peak for $CePd_3$. The presence of the peak was also indicated by Awashti *et al.*[41] using resonant cavities for three discrete frequencies (for an extensive review of optical properties of heavy-electron compounds, including Fermi-liquid aspects, see Ref. 42).

UPd_2Al_3 is a heavy-fermion material with a mass enhancement of 66.[43] The $5f$ moments order antiferromagnetically below 14.3 K,[44] and a superconducting phase coexisting with the magnetic order develops below 2 K. In the temperature range between these two transitions, the resistivity increases as T^2 with a typical coefficient $A \sim 1\mu\Omega$ cm/K^2, suggesting Fermi-liquid behavior of the charge carriers[45,46] with a $T_{\rm FL}$ of the order of 15 K. For this material, $\sigma(\omega)$ has been measured in the range from 0.002 to 1.3 cm^{-1} using a coaxial technique in Corbino geometry.[47] Figure 12 shows

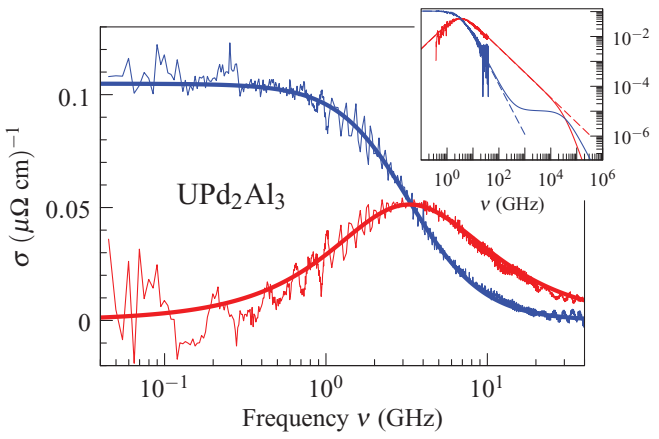

FIG. 12. (Color online) Microwave optical response of UPd_2Al_3 at $T = 2.75$ K. The thin lines show the measurements of Ref. 47. The solid lines show a fit to Eqs. (13) with the parameters $T_0 = 350$ K and $Z\Phi(0) = \epsilon_0(1.6 \times 10^{14}\ {\rm s}^{-1})^2$. (Inset) Same data on a wider frequency range. The dashed lines show the Drude model.

the microwave data of Ref. 47, measured at $T = 2.75$ K, well below $T_{\rm FL}$. The conductivity can be well fitted to the Drude model, Eq. (1), with the parameters $\sigma_{\rm dc} = 0.105\ (\mu\Omega\ {\rm cm})^{-1}$ and $\tau_{\rm D} = 4.7 \times 10^{-11}$ s. This led the authors to the conclusion that impurity scattering dominates in this frequency range. However, the extrapolated dc resistivity of ∼9 $\mu\Omega$ cm is of the order AT^2, which may also indicate that electron-electron scattering dominates the dc resistivity. As a matter of fact, the data can be equally well fitted to the Fermi-liquid formula (13), as show in Fig. 12. This provides an alternative interpretation for the success of the Drude model: the scattering rate is due to electron-electron interactions, but it is dominated by the temperature in this low-frequency range. At the experimental temperature $T = 2.75$ K, the thermal regime where deviations from the Drude model due to the frequency dependence of the scattering rate are expected is around $k_{\rm B}T/\hbar = 360$ GHz (inset of Fig. 12). Note that again $T_{\rm FL}$ is an order of magnitude smaller than the value $T_0 \sim 350$ K resulting from the fit in Fig. 12.

Recently, Nagel *et al.*[24] reported optical data for URu_2Si_2, exhibiting the $1/\tau_{\rm opt}(\omega,T) \propto (\hbar\omega)^2 + (p\pi k_{\rm B}T)^2$ dependence of the optical scattering rate with $p \approx 1$, i.e., well below $p = 2$ expected for a Fermi liquid [see Eq. (19)]. To our knowledge, the two cases in which a value of p closest to 2 has been observed are the κ-(BEDT-TTF)$_2$Cu[N(CN)$_2$]Br$_x$Cl$_{1-x}$ organic compound ($p \approx 2.4$)[48] and the underdoped $HgBa_2CuO_{4+\delta}$ ($p \approx 1.5$).[23] The optical conductivity of κ-(BEDT-TTF)$_2$Cu[N(CN)$_2$]Br$_x$Cl$_{1-x}$ does have a narrow Drude peak followed by a foot. However, the frequency region $\omega < \omega_{\rm L}$ has not been fully explored.

For most Fourier-transform spectrometers, the lower limit of the spectrometer range is about 20–40 cm^{-1}. As a result, experiments typically see only the upper frequency part of the shape shown in Fig. 2, containing the characteristic frequency scales $\omega_{\rm H}$, while the part of the spectrum around $\omega_{\rm L}$ is usually not reported. This upper frequency part is itself often approximated by a Drude form, which, however, should not be confused with the true low-frequency behavior of the conductivity. For a number of materials, the experimental reports have hinted toward a crossover to a low frequency regime that could be Fermi-liquid like. For example, in MnSi, the resistivity is found to follow $\rho = AT^2$ in the helimagnetic phase below 30 K, while the optical conductivity is given by $\sigma_1(\omega) \propto \omega^{-0.5}$ down to 30 cm^{-1}, even for data taken at 10 K, indicating that a crossover to Fermi-liquid like behavior, if present, would have to occur below 30 cm^{-1} (see Ref. 49).

This is remedied to a large extent by state of the art time-domain terahertz spectrometers, which typically span a frequency range from 1 up to 100 cm^{-1}. The limiting factor in the latter case is provided by diffraction in the long-wavelength limit, imposed by the finite sample size, which is typically of the order of a few squared millimeters. In Nb-doped $SrTiO_3$, T^2 resistivity in a broad temperature range is an indication for Fermi-liquid behavior.[50,51] Time-domain terahertz data reveal a very narrow zero-frequency mode,[52] similar to that in Fig. 2. On the other hand, whether or not the foot-shoulder at higher frequency is present in the data, has been impossible to establish because strong optical phonons mask the electronic part of the spectrum in the relevant frequency range.

A team involving the present authors recently reported Fermi-liquid like features for underdoped high-T_c cuprates in the pseudogap phase, in particular, the scaling collapse of the form $1/\tau_{\rm opt}(\omega,T) \propto (\hbar\omega)^2 + (p\pi k_{\rm B}T)^2$ for a broad range of ω and T.[23] Further analysis of these data in relation to the features discussed in the previous sections is under way.

The examples discussed in this section illustrate the experimental challenges that need to be met in order to establish in a single material the different aspects of the Fermi-liquid optical conductivity, such as the one displayed in Fig. 2. To the best of our knowledge, this is not available in the literature. Still, with appropriate choice of materials, sample geometry, and optical instrumentation, those challenges may ultimately be met.

VI. CONCLUSION

We have derived analytical formulas for the universal scaling laws that describe the optical response of local Fermi liquids. These laws depend on two variables, $\hbar\omega/(2\pi k_{\rm B}T)$ and $\omega\tau_{\rm qp} = \hbar\omega/(2\pi k_{\rm B}T)(T_0/T)$, where $\tau_{\rm qp}$ is the temperature-dependent quasiparticle relaxation time on the Fermi surface, and T_0 is a characteristic temperature, above which the scattering rate $\hbar/\tau_{\rm qp}$ is larger than $2\pi k_{\rm B}T$. In the most interesting temperature range, $T \ll T_0$, two regimes of frequency can be distinguished: $\hbar\omega \ll 2\pi k_{\rm B}T$ and $\hbar\omega \gtrsim 2\pi k_{\rm B}T$. In the former low-frequency regime, the conductivity displays a Drude-like response, with a saturation of the real part below the frequency $\tau_{\rm qp}^{-1}$, and a $1/\omega^2$ decay above $\tau_{\rm qp}^{-1}$. In the latter so-called "thermal" regime, clear signatures of FL behavior are identified, which are not contained in the simple Drude form. In particular, the Fermi liquid behaves inductively in the thermal regime, and the real part of the conductivity changes to a frequency dependence much weaker than $1/\omega^2$. The feature appears as a shoulder in a log-log plot, more as a foot in a linear plot of the conductivity. These scaling laws can help distinguishing among the ubiquitous deviations from Drude-like behavior those which prove FL behavior from those which disprove it. We have illustrated this by comparing the scaling forms with DMFT data for the Hubbard model at low doping. Finally, we have reviewed a number of experimental works, and concluded that, while hints of FL behavior have been reported, several of the characteristic features associated with the thermal regime remain to be observed.

ACKNOWLEDGMENTS

We acknowledge useful discussions with A. Chubukov, M. Dressel, A. J. Leggett, and T. Timusk, and are most grateful to M. Ferrero for discussions and for sharing his codes and his expertise on CT-QMC algorithms and analytical continuation methods. This work was supported by the Swiss National Science Foundation through Division II and MaNEP.

APPENDIX A: KUBO FORMULA FOR A LOCAL FERMI LIQUID

In general, the long-wavelength linear conductivity tensor is related to the current susceptibilities by the Kubo formula

$$\sigma_{\alpha\beta}(\omega) = \frac{ie^2}{\omega}[\chi_{\alpha\beta}(\omega) - \chi_{\alpha\beta}(0)]. \tag{A1}$$

$\chi_{\alpha\beta}(\omega)$ is the retarded macroscopic current-current correlation function, which may be obtained from the analytic continuation of the corresponding imaginary-time function:

$$\chi_{\alpha\beta}(i\Omega_n) = -\frac{1}{L^d}\int_0^{1/k_{\rm B}T} d\tau\, e^{i\Omega_n\tau}\langle j_\alpha(\boldsymbol{q}=0,\tau) j_\beta(\boldsymbol{0},0)\rangle, \tag{A2}$$

where L is the system size, d the dimensionality, $\boldsymbol{j}$ is the paramagnetic current operator, and $\Omega_n = 2n\pi k_{\rm B}T$ are the bosonic Matsubara frequencies. The diamagnetic contribution is real and diagonal and is commonly expressed in terms of the carrier density n and the carrier mass m, as $\chi_{\alpha\beta}(0) = -\delta_{\alpha\beta}(n/m)$. In interacting Fermi systems, the current susceptibilities can be formally represented by two classes of diagrams. The first class describes the propagation of uncorrelated particle-hole pairs, and can be summed to give the so-called "particle-hole bubble," formulated in terms of the single-particle spectral function $A(\boldsymbol{k},\varepsilon)$. The expression of the bubble is

$$\chi_{\alpha\beta}(\omega) = \frac{1}{L^d}\sum_{\boldsymbol{k}\sigma} v_{\boldsymbol{k}}^\alpha v_{\boldsymbol{k}}^\beta \int_{-\infty}^{\infty} d\varepsilon_1 d\varepsilon_2\, A(\boldsymbol{k},\varepsilon_1)A(\boldsymbol{k},\varepsilon_2) \times \frac{f(\varepsilon_1) - f(\varepsilon_2)}{\hbar\omega + i0^+ + \varepsilon_1 - \varepsilon_2}, \tag{A3}$$

where $f(\varepsilon)$ is the Fermi function and $\boldsymbol{v}_{\boldsymbol{k}} = (1/\hbar)\nabla E_{\boldsymbol{k}}$ is the group velocity with $E_{\boldsymbol{k}}$ the noninteracting electron dispersion. The second class of diagrams contains all processes involving interactions between the particle and the hole, the so-called "vertex corrections," which have been shown to vanish by symmetry in local Fermi liquids characterized by a momentum-independent self-energy.[13] This represents a considerable simplification, since the exact current-current correlation function reduces to Eq. (A3). For a local self-energy $\Sigma(\varepsilon) = \Sigma_1(\varepsilon) + i\,\Sigma_2(\varepsilon)$, the spectral function is

$$A(\boldsymbol{k},\varepsilon) = \frac{-\Sigma_2(\varepsilon)/\pi}{[\varepsilon - \xi_{\boldsymbol{k}} - \Sigma_1(\varepsilon)]^2 + [\Sigma_2(\varepsilon)]^2}, \tag{A4}$$

with $\xi_{\boldsymbol{k}} = E_{\boldsymbol{k}} - \mu$ and μ is the chemical potential. Inserting Eq. (A4) into Eq. (A3), taking the real part in Eq. (A1), and defining the isotropic conductivity as an average over the spatial coordinates, $\sigma(\omega) \equiv (1/d)\sum_{\alpha=1}^{d}\sigma_{\alpha\alpha}(\omega)$, directly leads to Eq. (8).

We note in passing that Eq. (8) provides an interesting generalization of the Drude formula for the dc conductivity: $\sigma_1(0)$ can be transformed into

$$\sigma_1(0) = \int_{-\infty}^{\infty} d\varepsilon\,[-f'(\varepsilon)]\frac{\hbar}{2|\Sigma_2(\varepsilon)|}\int_{-\infty}^{\infty} du \times \Phi(\varepsilon - \Sigma_1(\varepsilon) - u|\Sigma_2(\varepsilon)|)\frac{2/\pi}{(u^2+1)^2}, \tag{A5}$$

with f' the derivative of the Fermi function. Since Φ generally is a slow function of its argument, we may expand about $u = 0$, and get at lowest order,

$$\sigma_1(0) \approx \int_{-\infty}^{\infty} d\varepsilon\,[-f'(\varepsilon)]\frac{\hbar}{2|\Sigma_2(\varepsilon)|}\Phi(\varepsilon - \Sigma_1(\varepsilon)). \tag{A6}$$

If Φ is taken constant, we recover the well-known fact that the dc conductivity does not depend on the real part of the self-energy, explaining the absence of dynamical effective mass renormalization in the Drude formula. A weak dependence on the dynamical effective mass only enters through the energy dependence of the function $\Phi(\xi)$. It can also be seen that, if one expands $\Phi(\xi)$ in Eq. (8a), the first-order contribution to $\sigma_1(\omega)$ vanishes identically if the self-energy has the symmetry property $\Sigma(-\varepsilon) = -\Sigma^*(\varepsilon)$, as it is the case for the model Eq. (11).

The function $\Phi(\xi)$ in Eq. (8b) is generally a slowly-varying function of its argument. After replacing $\Phi(\xi)$ by $\Phi(0)$ in Eq. (8a), the ξ integration can be performed by means of the identity

$$\frac{1}{\pi}\int_{-\infty}^{\infty} d\xi \frac{\Gamma_1\Gamma_2}{\left[(\varepsilon_1-\xi)^2+\Gamma_1^2\right]\left[(\varepsilon_2-\xi)^2+\Gamma_2^2\right]} = \frac{\Gamma_1+\Gamma_2}{(\varepsilon_1-\varepsilon_2)^2+(\Gamma_1+\Gamma_2)^2}, \tag{A7}$$

leading to

$$\sigma_1(\omega) = \frac{\Phi(0)}{\omega}\int_{-\infty}^{\infty} d\varepsilon\,[f(\varepsilon)-f(\varepsilon+\hbar\omega)] \times \frac{-\Sigma_2(\varepsilon)-\Sigma_2(\varepsilon+\hbar\omega)}{[\hbar\omega+\Sigma_1(\varepsilon)-\Sigma_1(\varepsilon+\hbar\omega)]^2+[\Sigma_2(\varepsilon)+\Sigma_2(\varepsilon+\hbar\omega)]^2}. \tag{A8}$$

Equivalently, this can be rewritten as

$$\sigma_1(\omega) = \frac{\Phi(0)}{\omega}\int_{-\infty}^{\infty} d\varepsilon\,[f(\varepsilon)-f(\varepsilon+\hbar\omega)] \times \mathrm{Re}\left[\frac{i}{\hbar\omega+\Sigma^*(\varepsilon)-\Sigma(\varepsilon+\hbar\omega)}\right]. \tag{A9}$$

Equation (A9) shows that $\sigma_1(\omega)$ is given by Eq. (9). To prove that this is also the correct expression for $\sigma_2(\omega)$, we will show in the remainder of this section, that $\sigma(\omega)$ in Eq. (9) is an analytical function of the complex variable ω in the upper half of the complex plane and vanishes faster than $1/\omega$ for $|\omega| \to \infty$. Any function with these two properties satisfies Eq. (4), implying that Eq. (9) is the one and only function consistent with both Eqs. (4) and (A9).

We first note that the difference of Fermi functions in Eq. (9) is proportional to ω as $\omega \to 0$. Hence $\sigma(\omega)$ is analytic at $\omega = 0$. In order to get rid of the poles generated by the second Fermi function in Eq. (9), when continuing ω into the complex plane, we shift the integration variable in the second term, and rewrite the conductivity as

$$\sigma(\omega) = \frac{i\Phi(0)}{\omega}\int_{-\infty}^{\infty} d\varepsilon\, f(\varepsilon)\left[\frac{1}{\hbar\omega+\Sigma^*(\varepsilon)-\Sigma(\varepsilon+\hbar\omega)} - \frac{1}{\hbar\omega+\Sigma^*(\varepsilon-\hbar\omega)-\Sigma(\varepsilon)}\right]. \tag{A10}$$

The self-energy, like the Green's function, is analytic everywhere except possibly on the real axis, and decays at infinity provided that an asymptotic real value, corresponding to a shift of the chemical potential, is subtracted out. These analytic properties mean that the self-energy obeys

$$\Sigma(z) = \int_{-\infty}^{\infty} dE\,\frac{-\frac{1}{\pi}\mathrm{Im}\,\Sigma(E)}{z-E} = \int_{-\infty}^{\infty} dE\,(z^*-E)\frac{-\frac{1}{\pi}\mathrm{Im}\,\Sigma(E)}{|z-E|^2}. \tag{A11}$$

Here, z is a complex variable, and E is real. As a function of z, the self-energy has a branch-cut discontinuity on the real axis. The meaning of $\Sigma(E)$ in Eq. (A11) must therefore be disambiguated; when writing $\Sigma(E)$ with a real argument E, we actually mean $\Sigma(E+i0^+)$, i.e., the self-energy just above the real axis, which has the property $\mathrm{Im}\,\Sigma(E) < 0$. Since $\Sigma(z) \sim 1/z$ for $|z| \to \infty$, ω dominates as $|\omega| \to \infty$ in the denominator of both terms in Eq. (A10). This shows that $\sigma(\omega)$ decays at infinity faster than $1/\omega$. For a vanishing self-energy, both terms have a pole at $\omega = 0$. The analytical structure of the self-energy displaces the pole in the lower half of the complex plane. In order to see this, we can solve iteratively the equation giving the pole, i.e., $\hbar\omega = \Sigma(\varepsilon) - \Sigma^*(\varepsilon-\hbar\omega)$ and a similar expression for the first term in Eq. (A10), starting from the value $\omega_1 = 0$. From Eq. (A11) and the recursion relation $\hbar\omega_{j+1} = \Sigma(\varepsilon) - \Sigma^*(\varepsilon-\hbar\omega_j)$, we see that

$$\mathrm{Im}\,(\hbar\omega_{j+1}) = \mathrm{Im}\,\Sigma(\varepsilon) + \mathrm{Im}\,(\hbar\omega_j) \times \int_{-\infty}^{\infty} dE\,\frac{-\frac{1}{\pi}\mathrm{Im}\,\Sigma(E)}{|\varepsilon-\hbar\omega_j-E|^2}. \tag{A12}$$

The right-hand side is strictly negative if $\mathrm{Im}\,(\omega_j) \leqslant 0$, which means that the fixed point, if any, has $\mathrm{Im}\,(\omega) < 0$. Hence the analytic properties of the self-energy imply that the function in the square brackets in Eq. (A10) is analytic in the upper half of the complex ω plane.

APPENDIX B: OPTICAL SUM RULE FOR A SINGLE BAND

This Appendix provides a derivation of the sum rule given by Eqs. (3) and (10), valid for a single-band local Fermi liquid whose conductivity is given by Eq. (8). On the imaginary-frequency axis, the bubble contribution (A3) to the current-current correlation function takes a simple form in terms of the Green's function $\mathcal{G}(\boldsymbol{k},i\omega_n)$, with $\omega_n = (2n+1)\pi k_B T$ the fermionic Matsubara frequencies:

$$\chi_{\alpha\beta}(i\Omega_n) = \frac{k_B T}{L^d}\sum_{\boldsymbol{k}\sigma} v_{\boldsymbol{k}}^{\alpha} v_{\boldsymbol{k}}^{\beta} \sum_{i\omega_n} \mathcal{G}(\boldsymbol{k},i\omega_n)\mathcal{G}(\boldsymbol{k},i\omega_n+i\Omega_n). \tag{B1}$$

A convergence factor $e^{i\omega_n 0^+}$ is implied hereafter—if not explicitly written—in the Matsubara-frequency sums. In the complex plane, $\chi_{\alpha\beta}(z)$ has the same analytical structure as the self-energy in Eq. (A11). We therefore have

$$\chi_{\alpha\beta}(i\Omega_n = 0) = \frac{1}{\pi}\int_{-\infty}^{\infty} d\omega\,\frac{\mathrm{Im}\,\chi_{\alpha\beta}(\omega+i0^+)}{\omega}. \tag{B2}$$

Using this and the fact that $\mathrm{Im}\,\chi_{\alpha\beta}(\omega+i0^+)$ is an odd function of ω, we obtain from Eqs. (A1) and (B1),

$$\int_0^\infty d\omega\,\sigma_1(\omega) = -\frac{\pi e^2}{2d}\sum_{\alpha=1}^{d}\chi_{\alpha\alpha}(i\Omega_n=0) = -\frac{\pi e^2 k_B T}{2dL^d}\sum_{\boldsymbol{k}\sigma} v_{\boldsymbol{k}}^2 \sum_{i\omega_n}\mathcal{G}^2(\boldsymbol{k},i\omega_n). \quad \text{(B3)}$$

In a local Fermi liquid, the momentum dependence of the Green's function stems from the bare dispersion, $\mathcal{G}(\boldsymbol{k},i\omega_n)=1/[i\omega_n-\xi_{\boldsymbol{k}}-\Sigma(i\omega_n)]$, hence we have the property $\mathcal{G}^2(\boldsymbol{k},i\omega_n)=d\mathcal{G}(\boldsymbol{k},i\omega_n)/d\xi_{\boldsymbol{k}}$. The momentum sum in Eq. (B3) can then be converted into an energy integral involving $\mathcal{G}(\xi,i\omega_n)=1/[i\omega_n-\xi-\Sigma(i\omega_n)]$ as well as the transport function $\Phi(\xi)$ defined in Eq. (8b):

$$\int_0^\infty d\omega\,\sigma_1(\omega) = -\frac{\pi}{2}k_B T\sum_{i\omega_n}\int_{-\infty}^{\infty} d\xi\;\Phi(\xi)\frac{d\mathcal{G}(\xi,i\omega_n)}{d\xi}. \quad \text{(B4)}$$

The Matsubara-frequency sum of the Green's function gives the momentum distribution $k_B T\sum_{i\omega_n}\mathcal{G}(\xi,i\omega_n)e^{i\omega_n 0^+} = \int d\varepsilon f(\varepsilon)\,A(\xi,\varepsilon)\equiv n(\xi)$. Together with Eq. (3), this proves the first relation in Eq. (10). The second relation may be obtained by noting that $v_{\boldsymbol{k}}^2\mathcal{G}^2(\boldsymbol{k},i\omega_n)=(1/\hbar^2)[\nabla_{\boldsymbol{k}}\mathcal{G}(\boldsymbol{k},i\omega_n)]\cdot\nabla_{\boldsymbol{k}}\xi_{\boldsymbol{k}}$. Substituting this in Eq. (B3), and performing the momentum integration by parts, we arrive at

$$\int_0^\infty d\omega\,\sigma_1(\omega) = \frac{\pi e^2}{d\hbar^2}\frac{1}{L^d}\sum_{\boldsymbol{k}} n(\xi_{\boldsymbol{k}})\nabla^2\xi_{\boldsymbol{k}}, \quad \text{(B5)}$$

which leads to the second relation in Eq. (10).

APPENDIX C: CALCULATION OF THE $\mathscr{S}$ FUNCTION

In order to evaluate the $\mathscr{S}$ function, we use the exact representation

$$\frac{1}{e^{\pi(u-x)}+1}-\frac{1}{e^{\pi(u+x)}+1} = \frac{1}{\pi}\sum_{n=-\infty}^{+\infty}\left(\frac{1}{ip_n+x-u}-\frac{1}{ip_n-x-u}\right) \quad \text{(C1)}$$

with $p_n=2n+1$. Changing variable in the integral in Eq. (13), we see that each term with $p_n<0$ is equal to the corresponding term with $p_{-n-1}=-p_n>0$, so that the sum can be rewritten as a sum on $n\geqslant 0$. The integrations are elementary,

$$\frac{1}{\pi}\int_{-\infty}^{\infty} du\left(\frac{1}{ip_n+x-u}-\frac{1}{ip_n-x-u}\right)\times\frac{1}{1+x^2-iy+u^2} = \frac{i}{r(x,y)}\left[\frac{1}{p_n+r(x,y)+ix}-\frac{1}{p_n+r(x,y)-ix}\right],$$
$$r(x,y)=\sqrt{1+x^2-iy}, \quad \text{(C2)}$$

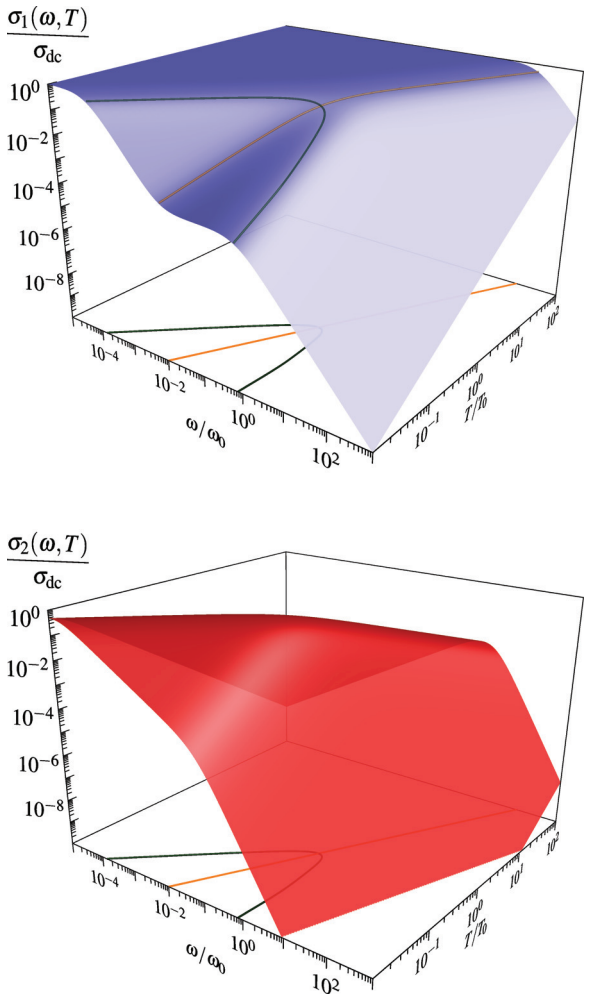

FIG. 13. (Color online) Real part (top) and imaginary part (bottom) of the optical conductivity normalized by the dc value, as a function of frequency and temperature. T_0 is defined in Eq. (11), and $\omega_0=2\pi k_B T_0/\hbar$. The straight orange lines indicate $\hbar\omega=2\pi k_B T$, and the green lines correspond to the dome in Fig. 3.

and we may recast the sums in terms of the digamma function $\psi(z)=\lim_{M\to\infty}[\ln M-\sum_{n=0}^{M}1/(n+z)]$, to finally get Eq. (13c).

Equation (14) shows that the conductivity normalized to the dc value is given by $\mathscr{S}(\frac{\omega/\omega_0}{T/T_0},\frac{\omega/\omega_0}{(T/T_0)^2})$. This is displayed as a function of frequency and temperature in Fig. 13. The function $\mathscr{S}$ is well approximated by the simple form $\mathscr{S}(x,y)\approx 1/(1+x^2-3iy/4)$ over the whole (x,y) plane.

APPENDIX D: COMPARING FERMI-LIQUID AND DRUDE FORMULA

In the Drude regime, defined by $\hbar\omega\ll 2\pi k_B T$ and $\omega\tau_{\mathrm{qp}}\sim 1$, the conductivity of a Fermi liquid is a universal function of $\omega\tau_{\mathrm{qp}}$ given by Eq. (15). This function is displayed in Fig. 14. The imaginary part σ_2 increases first linearly with a slope $1/2+3\zeta(3)/\pi^2\approx 0.865$, reaches a maximum at $\omega\tau_{\mathrm{qp}}\approx 1.162$, and then decreases as $12/\pi^2(\omega\tau_{\mathrm{qp}})^{-1}$. The real part decreases as $16/\pi^2(\omega\tau_{\mathrm{qp}})^{-2}$, and crosses the imaginary part at $\omega\tau_{\mathrm{qp}}\approx 1.198$, slightly above the point where σ_2 has its maximum. In the Drude model (1), σ_2 increases first like

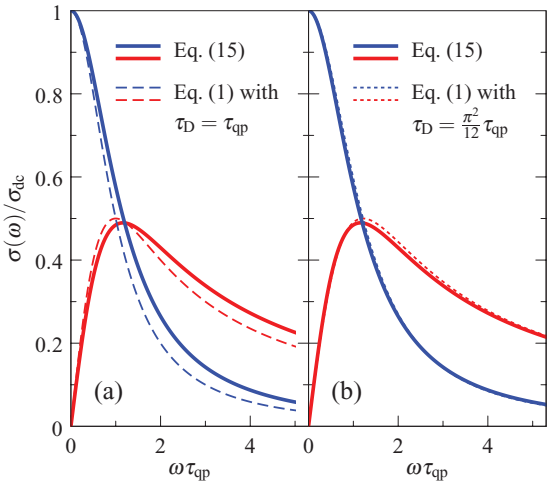

FIG. 14. (Color online) Comparison of the Fermi-liquid conductivity in the Drude regime, Eq. (15), with the Drude model (1). The solid blue and red lines show the real and imaginary parts of Eq. (15), respectively. The dashed lines in (a) show the Drude model assuming $\tau_D = \tau_{qp}$. The dotted lines in (b) show the Drude model assuming $\tau_D = (\pi^2/12)\tau_{qp}$ (see text).

$\omega\tau_D$, reaches a maximum at $\omega\tau_D = 1$, and then decreases as $(\omega\tau_{qp})^{-1}$; σ_1 decreases as $(\omega\tau_D)^{-2}$, and crosses σ_2 at its maximum.

When approximating the low-frequency response of a Fermi liquid by the Drude model, it is not possible to choose the time τ_D such that the four remarkable features—initial slope and maximum of σ_2, asymptotic decay of σ_1 and σ_2—are all described exactly. If one takes $\tau_D = \tau_{qp}$, none of these features is correctly reproduced, as illustrated in Fig. 14(a). Matching the initial slope of σ_2 in both models implies $\tau_D = 0.865\tau_{qp}$, matching the maximum of σ_2 means $\tau_D = \tau_{qp}/1.162$, matching the asymptotic decays of σ_1 and σ_2 leads respectively to $\tau_D = (\pi/4)\tau_{qp}$ and $\tau_D = (\pi^2/12)\tau_{qp}$. All four determinations of τ_D/τ_{qp} are close to 0.8. The choice $\tau_D = (\pi^2/12)\tau_{qp}$, because it gives the correct asymptotic decay of σ_2, also ensures that the spectral weight is the same in both models by the Kramers-Kronig relations. It is furthermore the closest to the average of the four determinations. Figure 14(b) shows a comparison of the Fermi-liquid model with the Drude model, assuming $\tau_D = (\pi^2/12)\tau_{qp}$.

APPENDIX E: MEMORY FUNCTION IN THE THERMAL AND DRUDE REGIMES

By solving Eq. (2) for $M(\omega)$, identifying $\sigma(\omega)$ with the Fermi-liquid result (13) and expanding for large $y = \omega\tau_{qp}$ with the help of Eq. (17), one arrives at the expression (21) for the memory function in the thermal regime. Inserting Eq. (21) back into Eq. (2), one recovers the generalized Drude form of Eqs. (18) and (19). From an experimental perspective, one sees in Eq. (21) that a plot of $\omega M_2(\omega)/[\omega + M_1(\omega)]$ in the region $\hbar\omega \sim 2\pi k_B T$ should allow to determine the parameter T_0.

We note that while the real part of M depends on the total spectral weight $\epsilon_0\omega_p^2$, the normalized imaginary part $M_2(\omega)/M_2(0)$ does not, since $M_2(\omega)/M_2(0) = \mathrm{Re}\,\sigma_{dc}/\sigma(\omega)$ as shown, e.g., in Eq. (7). Unlike $M_1(\omega)$, $M_2(\omega)/M_2(0)$ can therefore be determined accurately using a low-energy model. With the Fermi-liquid model (13), we have

$$\frac{M_2(\omega)}{M_2(0)} = \mathrm{Re}\,\frac{1}{\mathscr{S}(x,y)}. \tag{E1}$$

As $\lim_{y\to\infty} \mathrm{Re}[1/\mathscr{S}(x,y)] = (\pi/3)^2(1+x^2)$, one sees that the scaling function for $M_2(\omega)$ in the thermal regime extrapolates to the value $(\pi/3)^2 M_2(0)$ at $\omega = 0$, as can be seen in Fig. 5.

The behavior of $M_2(\omega)/M_2(0)$ in the Drude regime $\omega\tau_{qp} < 1$ is quadratic and given by

$$\frac{M_2(\omega)}{M_2(0)} = 1 + (\omega\tau_{qp})^2\left[a + b\left(\frac{T}{T_0}\right)^2\right], \tag{E2}$$

where a and b are the numerical constants $a = 1/8 + \pi^2/80 - 3\zeta(3)/(4\pi^2) - (3\zeta(3)/\pi^2)^2 \approx 0.0235$ and $b = 1/2 + \pi^2/60 + 3\zeta(3)/\pi^2 \approx 1.03$. This is plotted in Fig. 5(a) as the thin line.

APPENDIX F: IMPURITY SCATTERING, ROBUSTNESS OF THE 2π FACTOR

In this Appendix, we show that the inclusion of a constant scattering rate $-i\Gamma$ in the Fermi-liquid self-energy (11) does not change the scaling of the optical conductivity in the thermal regime. A frequency-independent scattering rate can crudely describe the effect of impurity scattering. On adding $-i\Gamma$ to the self-energy, the only change induced in Eq. (13) occurs in the expression of the function $\mathscr{S}$: in the denominator of the integrand, 1 is replaced by $1 + 2Z\tau_{qp}\Gamma/\hbar$. The correction term $\sim\Gamma/T^2$ is the ratio between the impurity and the electron-electron scattering rates. This change can be absorbed into a redefinition of the variable y:

$$y = \frac{\bar{\omega}}{\bar{T}^2} \to y_1 + iy_2 = \frac{\bar{\omega} + iZ\Gamma/(\pi k_B T_0)}{\bar{T}^2}. \tag{F1}$$

The same modification made in the analytical form (13c) yields the scaling function in the presence of impurity scattering. It should be noted that, with this modification, the function $\mathscr{S}$ is not unity in the dc limit, and therefore the dc conductivity is different from σ_{dc} as defined in Eq. (13). In particular, the residual dc resistivity can be evaluated as $\rho_0 = 2\Gamma/[\hbar\Phi(0)]$.

If $\omega \gg 2Z\Gamma/\hbar$, we can expand in the thermal regime like in Eq. (17), which must then be replaced by

$$\mathscr{S}(x, y_1 \to \infty, y_2) = \frac{12i}{\pi^2 y_1} + \frac{16}{\pi^2 y_1^2}\left(1 + x^2 + \frac{3}{4}y_2\right). \tag{F2}$$

Consequently, we find that the optical scattering rate reflects the increased quasiparticle scattering rate (with an extra factor of two), but that the frequency-temperature scaling is

unchanged:

$$\frac{\hbar}{\tau_{\rm opt}(\omega)} = \frac{2}{3\pi k_{\rm B} T_0}[(\hbar\omega)^2 + (2\pi k_{\rm B} T)^2] + 2Z\Gamma. \quad \text{(F3)}$$

The impurity scattering, however, reduces the frequency-temperature domain below the dome in Fig. 3, where $\tau_{\rm opt}(\omega) > 1/\omega$. The equation of the dome in the presence of impurity scattering is

$$T_1(\omega) = T_0\sqrt{\frac{3}{4}\left(\bar{\omega} - \frac{Z\Gamma}{\pi k_{\rm B} T_0}\right) - \bar{\omega}^2}. \quad \text{(F4)}$$

Hence the dome disappears—and consequently the shoulder in the log-log plot of $\sigma_1(\omega)$—if $Z\Gamma > 3\pi k_{\rm B} T_0/16$.

[1] P. Drude, Ann. Phys. **306**, 566 (1900).
[2] M. Dressel and M. Scheffler, Ann. Phys. (Leipzig) **15**, 535 (2006).
[3] L. Landau, Zh. Eksp. Teor. Fiz. **30**, 1058 (1956) [Sov. Phys. JETP **3**, 920 (1957)].
[4] A. V. Chubukov and D. L. Maslov, Phys. Rev. B **86**, 155136 (2012).
[5] D. L. Maslov and A. V. Chubukov, Phys. Rev. B **86**, 155137 (2012).
[6] M. C. Nuss and J. Orenstein, in *Millimeter and Submillimeter Spectroscopy of Solids*, Topics in Applied Physics, Vol. 74, edited by G. Grüner (Springer, New York, 1998), pp. 7–50.
[7] *Terahertz Spectroscopy: Principles and Applications*, edited by S. L. Dexheimer (CRC Press, Boca Raton, 2007).
[8] W. Metzner and D. Vollhardt, Phys. Rev. Lett. **62**, 324 (1989).
[9] E. Müller-Hartmann, Z. Phys. B **76**, 211 (1989).
[10] D. N. Basov, R. D. Averitt, D. van der Marel, M. Dressel, and K. Haule, Rev. Mod. Phys. **83**, 471 (2011).
[11] W. Götze and P. Wölfle, Phys. Rev. B **6**, 1226 (1972).
[12] A. Georges and G. Kotliar, Phys. Rev. B **45**, 6479 (1992).
[13] A. Khurana, Phys. Rev. Lett. **64**, 1990 (1990).
[14] W. Lee, D. Rainer, and W. Zimmermann, Physica C **159**, 535 (1989).
[15] S. V. Shulga, O. V. Dolgov, and E. G. Maksimov, Physica C **178**, 266 (1991).
[16] P. B. Allen, arXiv:cond-mat/0407777.
[17] One sees the following from Eq. (18): $\sigma_2 \sim 1/[\omega + \tau_{\rm opt}^{-2}(\omega)/\omega]$. Hence the $1/\omega^3$ results from the ω^2 of the optical scattering rate. At frequencies well above $\omega_\pm$ (defined in Sec. IV), $\tau_{\rm opt}^{-1}$ is expected to saturate to a frequency-independent value, so that the correct asymptotic $1/\omega$ decay of σ_2 is recovered. The saturation of $\tau_{\rm opt}^{-1}$ does not affect the power law of σ_1, since it can be seen to go like $1/[\omega^2\tau_{\rm opt}(\omega) + \tau_{\rm opt}^{-1}(\omega)]$.
[18] R. N. Gurzhi, Sov. Phys. JETP **35**, 673 (1959), and references therein.
[19] P. E. Sulewski, A. J. Sievers, M. B. Maple, M. S. Torikachvili, J. L. Smith, and Z. Fisk, Phys. Rev. B **38**, 5338 (1988).
[20] T. Katsufuji and Y. Tokura, Phys. Rev. B **60**, 7673 (1999).
[21] J. Yang, J. Hwang, T. Timusk, A. S. Sefat, and J. E. Greedan, Phys. Rev. B **73**, 195125 (2006).
[22] M. Dressel, J. Phys.: Condens. Matter **23**, 293201 (2011).
[23] S. I. Mirzaei, D. Stricker, J. N. Hancock, C. Berthod, A. Georges, E. van Heumen, M. K. Chan, X. Zhao, Y. Li, M. Greven, N. Barišić, and D. van der Marel, Proc. Natl. Acad. Sci. USA (to be published), arXiv:1207.6704.
[24] U. Nagel, T. Uleksin, T. Rõõm, R. P. S. M. Lobo, P. Lejay, C. C. Homes, J. S. Hall, A. W. Kinross, S. K. Purdy, T. Munsie, T. J. Williams, G. M. Luke, and T. Timusk, Proc. Natl. Acad. Sci. USA **109**, 19161 (2012).
[25] A. Georges, G. Kotliar, W. Krauth, and M. J. Rozenberg, Rev. Mod. Phys. **68**, 13 (1996).
[26] M. Jarrell, J. K. Freericks, and T. Pruschke, Phys. Rev. B **51**, 11704 (1995).
[27] J. Merino, M. Dumm, N. Drichko, M. Dressel, and R. H. McKenzie, Phys. Rev. Lett. **100**, 086404 (2008).
[28] E. Gull, A. J. Millis, A. I. Lichtenstein, A. N. Rubtsov, M. Troyer, and P. Werner, Rev. Mod. Phys. **83**, 349 (2011).
[29] M. Ferrero and O. Parcollet, TRIQS: a Toolbox for Research on Interacting Quantum Systems (http://ipht.cea.fr/triqs).
[30] R. Bulla, T. A. Costi, and T. Pruschke, Rev. Mod. Phys. **80**, 395 (2008).
[31] R. Žitko, NRG Ljubljana: open source numerical renormalization group code (http://nrgljubljana.ijs.si).
[32] X. Deng, J. Mravlje, R. Žitko, M. Ferrero, G. Kotliar, and A. Georges, Phys. Rev. Lett. **110**, 086401 (2013).
[33] M. J. Rozenberg, G. Kotliar, and H. Kajueter, Phys. Rev. B **54**, 8452 (1996).
[34] J. Merino and R. H. McKenzie, Phys. Rev. B **61**, 7996 (2000).
[35] A. Comanac, L. de' Medici, M. Capone, and A. J. Millis, Nat. Phys. **4**, 287 (2008).
[36] N. Lin, E. Gull, and A. J. Millis, Phys. Rev. B **80**, 161105 (2009).
[37] N. Lin, E. Gull, and A. J. Millis, Phys. Rev. B **82**, 045104 (2010).
[38] D. Bergeron, V. Hankevych, B. Kyung, and A.-M. S. Tremblay, Phys. Rev. B **84**, 085128 (2011).
[39] M. M. Zemljič and P. Prelovšek, Phys. Rev. B **72**, 075108 (2005).
[40] B. C. Webb, A. J. Sievers, and T. Mihalisin, Phys. Rev. Lett. **57**, 1951 (1986).
[41] A. M. Awasthi, W. P. Beyermann, J. P. Carini, and G. Grüner, Phys. Rev. B **39**, 2377 (1989).
[42] L. Degiorgi, Rev. Mod. Phys. **71**, 687 (1999).
[43] C. Geibel, C. Schank, S. Thies, H. Kitazawa, C. D. Bredl, A. Böhm, M. Rau, A. Grauel, R. Caspary, R. Helfrich, U. Ahlheim, G. Weber, and F. Steglich, Z. Phys. B **84**, 1 (1991).
[44] A. Krimmel, P. Fischer, B. Roessli, H. Maletta, C. Geibel, C. Schank, A. Grauel, A. Loidl, and F. Steglich, Z. Phys. B **86**, 161 (1992).
[45] K. Ghosh, S. Ramakrishnan, and G. Chandra, Phys. Rev. B **47**, 8305 (1993).
[46] F. Wastin, E. Bednarczyk, and J. Rebizant, J. Alloys Compd. **271**, 437 (1998).
[47] M. Scheffler, M. Dressel, M. Jourdan, and H. Adrian, Nature (London) **438**, 1135 (2005).
[48] M. Dumm, D. Faltermeier, N. Drichko, M. Dressel, C. Mézière, and P. Batail, Phys. Rev. B **79**, 195106 (2009).
[49] F. P. Mena, D. van der Marel, A. Damascelli, M. Fäth, A. A. Menovsky, and J. A. Mydosh, Phys. Rev. B **67**, 241101(R) (2003).
[50] S. N. Klimin, J. Tempere, D. van der Marel, and J. T. Devreese, Phys. Rev. B **86**, 045113 (2012).
[51] D. van der Marel, J. L. M. van Mechelen, and I. I. Mazin, Phys. Rev. B **84**, 205111 (2011).
[52] J. L. M. van Mechelen, D. van der Marel, C. Grimaldi, A. B. Kuzmenko, N. P. Armitage, N. Reyren, H. Hagemann, and I. I. Mazin, Phys. Rev. Lett. **100**, 226403 (2008).